Seasonal Heat Transport in a Primitive Equations Model of the Tropical Indian Ocean

S. WACONGNE

Laboratoire de Physique des Océans UMR, CNRS/IFREMER/UBO, Université Bretagne Occidentale, Brest, France

R. PACANOWSKI

Geophysical Fluid Dynamics Laboratory/NOAA, Princeton, New Jersey

(Manuscript received 3 August 1995, in final form 18 April 1996)

ABSTRACT

This work analyzes seasonal heat transport in an ocean-only numerical simulation of the Indian Ocean forced by realistic seasonal winds and surface heat fluxes north of 15°S, assuming no Indonesian Throughflow. The seasonal changes in the model circulation and temperature structure are found to be overall consistent with observations, despite flaws in sea surface temperature and mixed layer depth. The simulation confirms that the reversal of the monsoons and of the associated Ekman transports plays an important role in reversing the sign of the ocean heat transport seasonally causing, in particular, the Arabian Sea's drastic annual cooling, but it suggests that, south of 10°N, deep boundary currents must reverse as well. Most of the model heat transport is carried by a deep downwelling cell during the northeast monsoon and by a shallower upwelling cell during the southwest monsoon. An analysis of the three-dimensional circulation reveals that, in boreal summer, the net -1.2 pW (1 pW = 10^{15} W) cross-equatorial model heat transport derives mostly from a 20×10^6 m^3 s^{-1} northward boundary current at intermediate levels (12.5°C) returned over the interior at the surface (27.5°C). In boreal winter, the net $+1$ pW heat transport derives mostly from a 10×10^6 m^3 s^{-1} northward interior surface flow (27.5°C) returned in several deep southward boundary currents (5°C). It is argued that the $+1$ pW February heat transport value is realistic and that a deep overturning cell must therefore exist, otherwise the return branch of the relatively small February Ekman transport would have to occur at a negative transport-averaged temperature. Moreover, deep downwelling during the northeast monsoon occurs in the model because of a pattern of flow convergence at intermediate levels of the Somali Current that is consistent with direct observations. An approach toward assessing the location and the role of diabatic processes (which could be responsible for too deep a penetration of the downwelling cell) is tested, and a formal decomposition of the seasonal heat transport into diabatic and adiabatic components is suggested. Representing as a function of latitude and potential temperature an equivalent streamfunction associated with diffusion appears a promising step toward quantifying such diabatic heat transports on a seasonal basis.

1. Introduction

The monsoonal wind system over the northern and equatorial Indian Ocean drives spectacular seasonal variations, especially visible in the annual reversal of the Somali Current, in the semiannual occurrence of strong equatorial surface jets, and in the abrupt annual cooling of the Arabian Sea [decrease in heat content and surface temperature, Düing and Leetmaa (1980)]. This cooling occurs during the southwest monsoon in boreal summer, that is, at a time of net surface heat flux into the ocean, which in other parts of the Northern Hemisphere would coincide with warming. The ocean circulation, characterized in boreal summer by strong coastal upwelling in the Somali Current region and southeastward Ekman flow in the interior, must therefore play a major role in exporting heat out of the Arabian Sea during the southwest monsoon (Figs. 1b,d,f).

This point is supported by the work of Hastenrath and Greischar (1993), who made an indirect estimate of the seasonal cycle of meridional oceanic heat transport by subtracting monthly estimates of the time variation of upper oceanic heat content from monthly estimates of atmospheric fluxes at the ocean surface (and integrating southward from the northern boundary). In agreement with an earlier estimate by Hsiung et al. (1989), they find southward oceanic heat transport in boreal summer and northward transport in boreal winter (i.e., a heat transport always toward the winter hemisphere, enhanced during boreal summer). There exists no direct oceanic estimate of this seasonal reversal in the direction of heat transport. Estimates from zonal transoceanic hydrographic sections have been made at 32°S, where seasonal variations are much less conspicuous, and they have been considered estimates of the mean. Thus, Toole and Warren (1993) recently

Corresponding author address: Dr. S. Wacongne, Laboratoire de Physique des Océans, UBO/Faculté des Sciences et Techniques, 6, Avenue Le Gorgeu, BP 809, Brest, Cedex 29285, France.
E-mail: sophie.wacongne@deneb-gw.univ-brest.fr

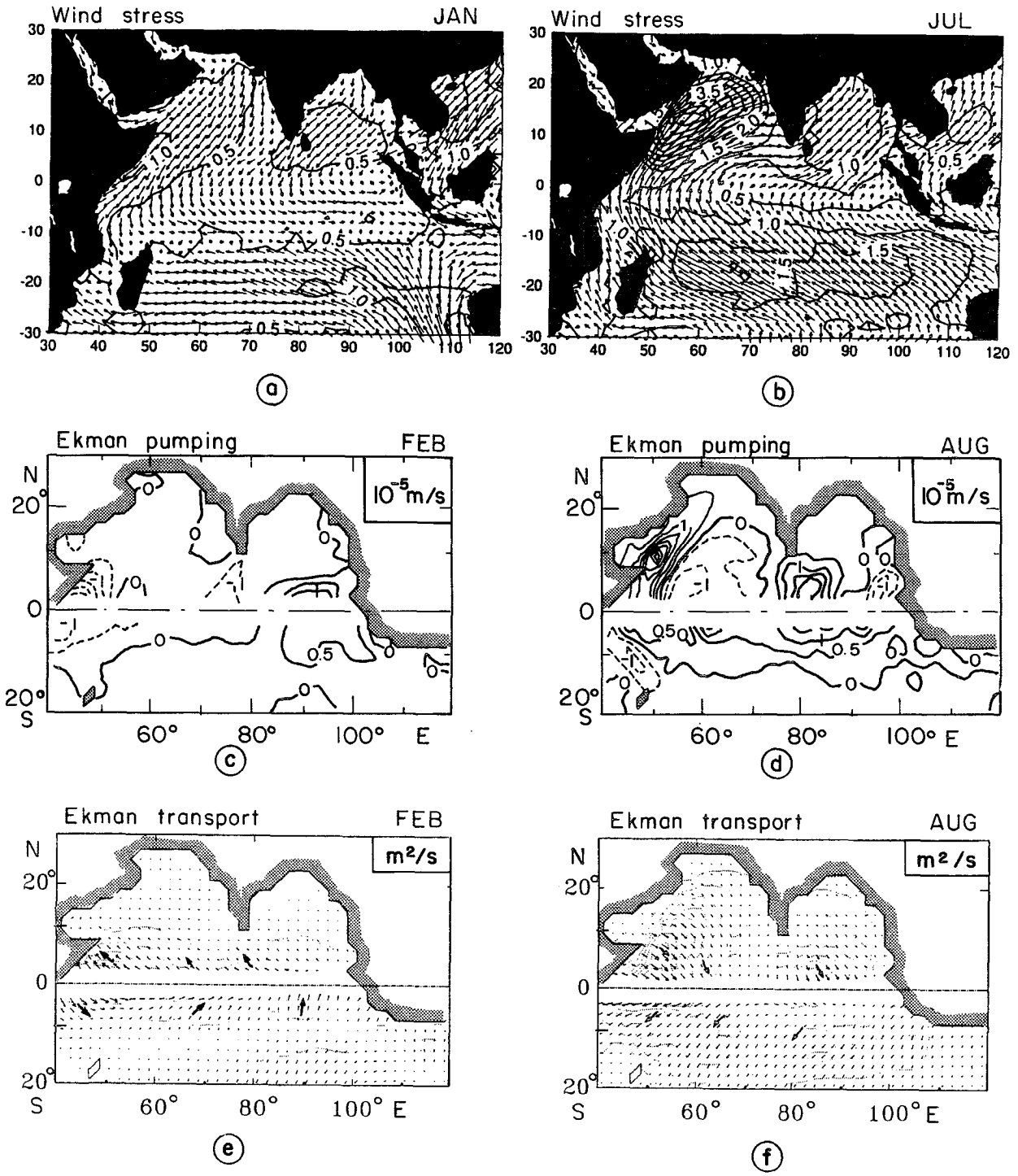

FIG. 1. Wind forcing at the peak of the northeast monsoon (Jan–Feb, left panels) and at the peak of the southwest monsoon (Jul–Aug, right panels). The upper panels (a–b), redrawn after Rao et al. (1989), show the wind stress (contours of its norm every 0.5×10^{-1} N m^{-2}); the middle panels (c–d) the Ekman pumping (contours 0.5×10^{-5} m s^{-1}); and the lower panels (e–f) the Ekman transport (contours of its norm every 2 m^2 s^{-1}). Note (emphasized arrows) that because of the veering of the wind stress at the crossing of the equator (change of sign of the zonal component) the tropical Ekman transport in both hemispheres is to the north over most of the basin in February and to the south in August.

estimated a net annual divergence of about 1 pW,[1] which agrees at least in sign and order of magnitude with estimates of the yearly net energy influx at the surface north of 32°S.

Ekman transport, which carries the warmest temperatures of the water column and which reverses to the northwest during the northeast monsoon (Figs. 1a,c,e), can play a decisive role in reversing the sign of the net heat transport at that season, at least north of 10°S where the Indian Ocean is most influenced by the monsoon (Levitus 1987). Moreover, this sign reversal of heat transport can occur mostly adiabatically. This will be the case if, in order to accommodate the warm northward Ekman transport and its necessarily colder southward return flow, the volume of warm water increases, the volume of cold water decreases (i.e., the isotherms deepen), but negligible temperature conversion takes place. In reality, some conversion of warm to cold water, that is, some cross-isotherm flux, must occur somewhere in the domain in boreal winter, tempering isotherm deepening and contributing to the northward heat transport, because the net surface heat flux is negative (out of the ocean). This illustrates that, when dealing with seasonal variations in heat transport, one deals with two components: an "adiabatic" and a "diabatic" heat transport, easily defined formally but hard to separate in practice because changes in heat content reflect both adiabatic and diabatic processes. (By contrast, the annual mean heat transport can be thought of as purely diabatic.)

Which components of the Indian Ocean circulation actually achieve the net oceanic heat transport on a seasonal basis? Is it indeed essential that the Ekman transport reverses direction seasonally? How is heat transported across the equator? What are the adiabatic and diabatic components of the heat transport? Which varies most from one monsoon season to the other? Where do temperature conversions mostly occur? These are questions that one cannot address using present oceanic observations but that one can explore using numerical simulations. Hence, the motivation for this study.

The simulation of a tropical Indian Ocean reported on here, with no Indonesian Throughflow, was run in 1985 by Philander and Pacanowski at GFDL, Princeton, to study the seasonal cycle of the upper layers. Model topography and model grid are presented in Fig. 2. This simulation is among the first to be based upon a fully nonlinear stratified model and realistic climatological forcing. It has been used to study certain limited aspects of the circulation (Schott 1986; Schott et al. 1988; Visbeck and Schott 1992), but no analysis of the overall model performance has yet been published. We chose to work with this rather old model because of its availability to us. As is the case for simpler models, the performance of this one suffers from limited resolution, crude parameterizations of small-scale processes, and uncertainties in the dynamical and thermodynamical forcing fields. The model has at its disposal, however, a rich range of physical mechanisms that govern large-scale dynamics. Despite known deficiencies (constant nonpenetrative shortwave input, primitive mixed layer physics, unrealistic freshwater budget), it does deal with diabatic processes, so that its use is more relevant to the questions addressed here than the use of a simpler reduced-gravity model, which could only hope to reproduce the adiabatic part of the total heat transport. Finally, the simulated seasonal cycles of surface currents and oceanic meridional heat transport qualitatively agree with observed estimates. The mechanisms controlling these seasonal variations in the model appear physically plausible and relatively insensitive to the model defects. We believe these mechanisms will prove relevant in more advanced models and in the real world.

For the readers familiar with the GFDL model, it may be enough to know that the version used to generate the run studied here is the same primitive equations 27-level model used by Philander and Pacanowski (1986a,b) and by Philander et al. (1987) to study the seasonal cycles of the tropical Atlantic and Pacific, respectively (same code, same parameterizations). For the other readers, the simulation and its limitations are presented in more detail in appendix A. The model was spun up for two years and integrated for another three years, a time purposefully short compared to the timescale for thermodynamic adjustment, but long enough for the upper tropical circulation to have reached a repeatable seasonal cycle. For all analyses below, an output of instantaneous fields on the 15th of each month of the last year of integration was used. Because the forcings are based on monthly averaged quantities and given past experience with similarly forced instantaneous and monthly averaged fields in the tropical Atlantic, we actually expect these instantaneous fields to be fairly representative of monthly averages. The coarse temporal resolution of this output, however, did not allow any decomposition into mean and eddy (or into annual mean, monthly mean, and eddy) fields. We will be looking at seasonal variations of instantaneous fields and, whenever referring to annual means, we will be talking about estimates obtained from averaging 12 instantaneous values.

In section 2, we show how the model circulation compares with ship drift estimates and with the few direct observations of subsurface currents; we diagnose the seasonal cycle of the model zonally integrated heat budget and compare it with observational estimates. Section 3 shows how, in the model, heat is transported predominantly by the zonally integrated circulation, which exhibits spectacular changes between February and August. This leads us to explore which seasonal changes in the model's three-dimensional circulation cause the changes in the meridional streamfunction, and discover that reversals in deep boundary currents

[1] 1 pW = 10^{15} W.

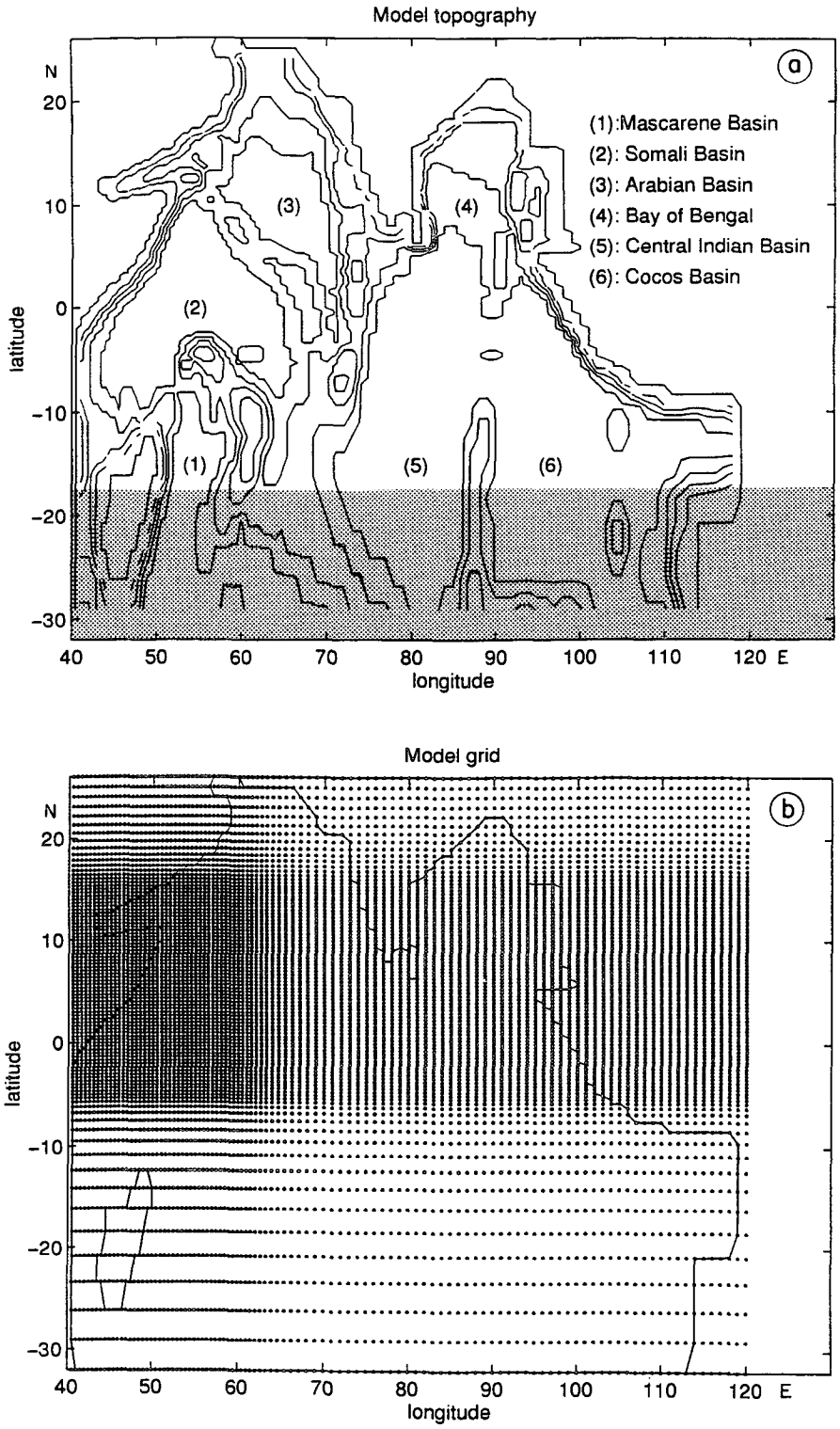

FIG. 2. Topography (a) (contour interval 1000 m) and horizontal grid (b) for the Indian Ocean model. The shaded region south of 18°S on (a) represents the relaxation layer.

are involved. Section 4 discusses the possible relevance of the simulation to the real Indian Ocean. We reexamine discrepancies between model and observations on the annual mean, seasonal reversals in observed deep currents, and indirect estimates of the seasonal heat transport; we explore the respective parts played by adiabatic and diabatic processes in the model seasonal heat transport; and we speculate on the possible impact of having blocked the Indonesian Throughflow. Appendix B formalizes the problem of decomposing the heat transport into its adiabatic and diabatic components.

The spirit of this work is to provide a benchmark for future comparison with more recent and more sophisticated simulations as well as with upcoming observations. We are not trying to defend the 1985 simulation and the parameterizations chosen at the time it was run. We will, in fact, insist on aspects of that simulation that need improving as much as on its robust features. Some of the nontraditional diagnostics that we developed to address the questions posed above may appear somewhat far fetched when applied to the 1985 run (admittedly not especially designed to address these questions). We nevertheless insist on the analysis because it greatly helped our own reflection on seasonal heat transport and because we believe it will provide a useful framework within which to study and intercompare other simulations. [For a review of simulations of the Indian Ocean, the reader is referred to McCreary et al. (1993) and to Godfrey et al. (1995).]

2. Model assessment

a. Circulation

Monthly instantaneous vector plots of the model horizontal circulation at the 5-m level were averaged within 2° latitude by 5° longitude boxes between 20°S and 20°N to obtain the same resolution as the Richardson and McKee (1989) monthly mean maps of ship drifts. Figure 3 presents the comparison for months typical of the developed monsoons: February (northeast monsoon) and August (southwest monsoon), and for months typical of the intermonsoon seasons: May and November. Overall, the two sets of maps compare remarkably well in speed, direction, and seasonal variations. This is true, in particular, for the seasonal reversals of the Somali Current along the western boundary and those of the Monsoon Drift Current south of Sri Lanka in response to the monsoons reversals, for the convergence of the southward Somali Current and the northward East African Coastal Current into an eastward South Equatorial Countercurrent during the northeast monsoon, for the appearance of the eastward equatorial jets along the equator during the transition between monsoons,[2] for the direction of rotation of the large-scale flow in the Arabian Sea and the Bay of Bengal, and for the southeastward current south of Indonesia.

An apparent discrepancy can be noted year-round south of 5°S in the westward South Equatorial Current, where the model simulation at 5 m shows a stronger southward component of flow than observed. (This contributes at 3°–10°S to a model East African Coastal Current that is weaker than observed.) Paradoxically, this discrepancy is not present in the Woodberry et al. (1989) simulation of the southern tropical Indian Ocean by a simpler nonlinear reduced gravity model. This behavior of the GFDL model (also visible in simulations of the tropical Atlantic and Pacific Oceans by the GFDL and other general circulation models) appears to be a consequence of its thermodynamics. In regions where the mixed layer depth is not determined dynamically, the model underestimates it because the shortwave radiation (constant in the model, see appendix A), being nonpenetrative, restricts the mixed layer thickness to the uppermost model level, that is, to a layer 10 m thick where all the Ekman transport (to the southwest in this region) is concentrated (cf. Figs. 3a,b to Figs. 1e–f near 10°S). Allowing seasonal variations in shortwave radiation and introducing high-frequency wind variability would also contribute to improved mixed layer thickening. Ocean general circulation models with mixed layer physics do simulate surface currents more satisfactorily (e.g., Rosati and Miyakoda 1988). The comparison with the observations (and with models with a coarser vertical resolution or devoid of diabatic processes) improves if one considers, instead of just the first model level, an average of the two or three upper levels; that is, if one effectively redistributes the surface momentum over a deeper (20–30 m thick) layer. Contrasting the nonaveraged model surface velocity with finer-scale observations (not shown) again reveals that the model reproduces the large eddy structure of the surface Somali Current less satisfactorily than simpler reduced gravity simulations. As before, the comparison improves as soon as one considers the average of the two or three upper model levels.

Other systematic discrepancies of relatively small scale exist, probably related to the neglect of the Indonesian Throughflow and/or to inadequacies in the southern boundary condition. The year-round flow between Africa and Madagascar is southward (toward the Agulhas Current) in the ship drift maps [see also Swallow et al. (1991)], but northward at 5 m in the model. In August at the eastern end of 10°S, the model simulates a much weaker current south of Indonesia than the one shown by the ship drift map.

Few direct observations of subsurface currents exist within the simulated domain north of 15°S. Most concern either the equatorial region [e.g., Luyten and Swallow (1976) for the deep jets; Leetmaa and Stommel (1980) for the equatorial undercurrent or the Somali Current (e.g., Schott et al. 1989, 1990)]. Within the limits of its resolution, the model compares favor-

[2] See also Visbeck and Schott (1992), their Fig. 4.

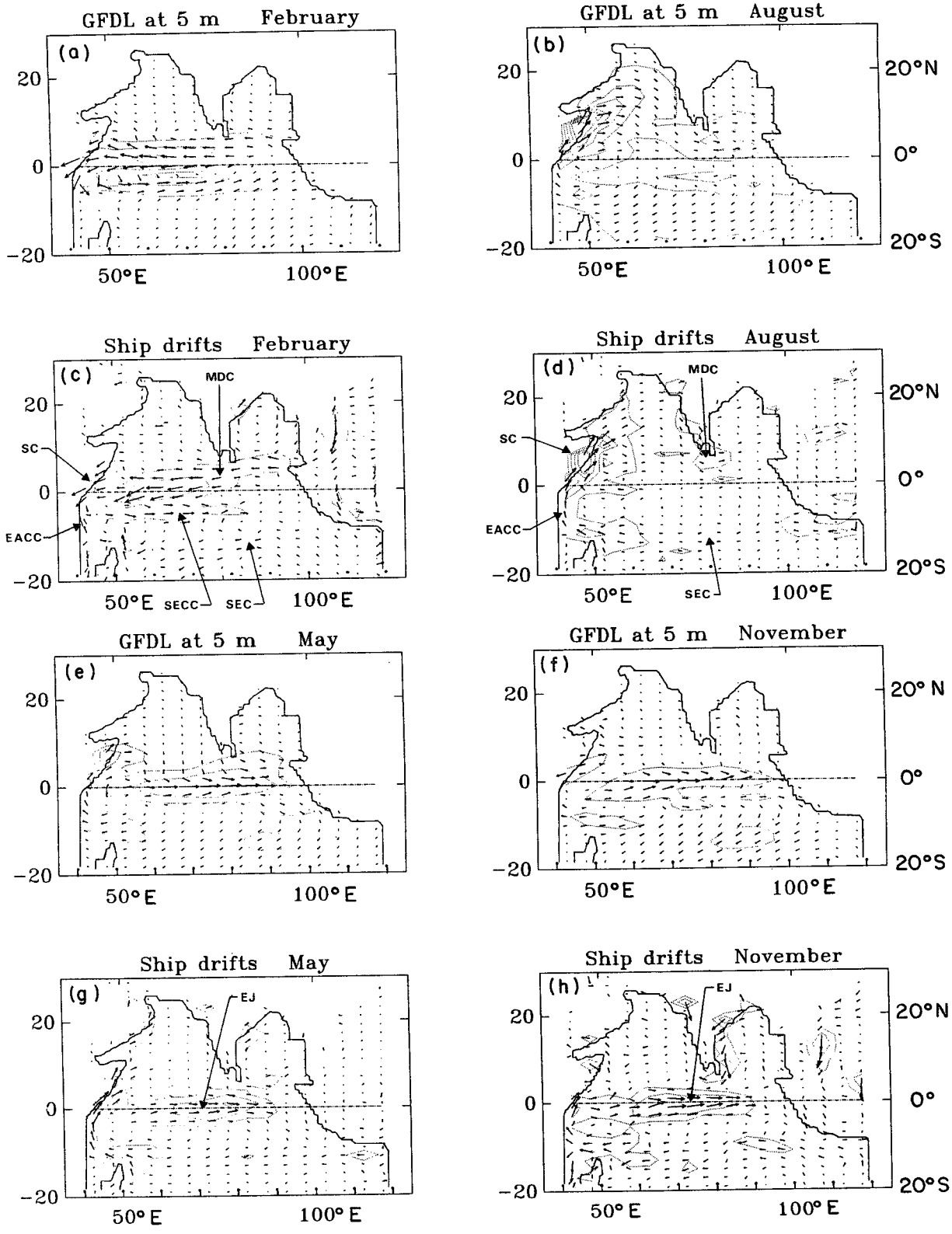

FIG. 3. Contrast between model currents (a), (b), (e), (f) at the first (5 m) vertical level and ship drift currents (c), (d), (g), (h) from Richardson and McKee's (1989) climatology, for February, during the northeast monsoon (a)–(c); August, during the southwest monsoon (b)–(d); and for May (e)–(g) and November (f)–(h), the transition seasons between monsoons. Contours represent the norm of the velocity vector every 0.25 m s^{-1}. SEC: South Equatorial Current, SECC: South Equatorial Countercurrent, EACC: East African Countercurrent, SC: Somali Current, MDC: Monsoon Drift Current, and EJ: equatorial jet.

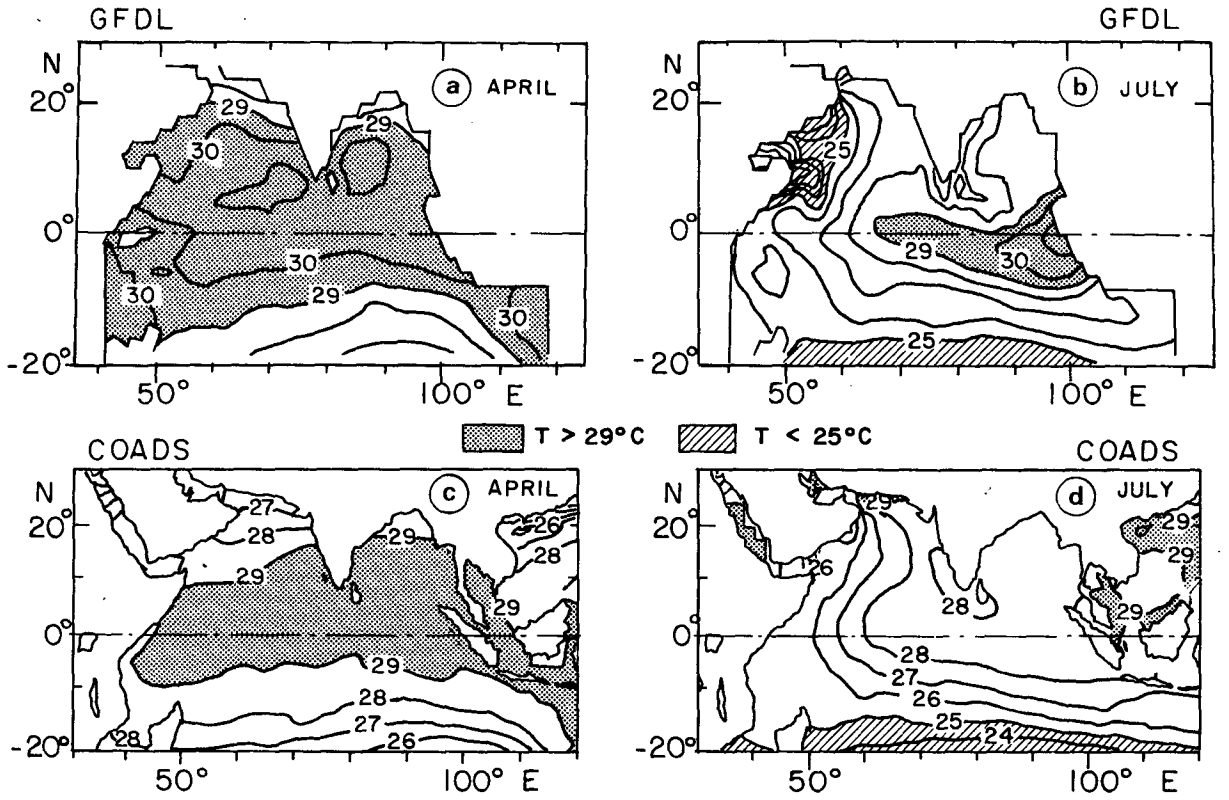

FIG. 4. Contrast between model temperature at the first (5 m) vertical level (upper panels) and COADS climatology (lower panels), redrawn after Rao et al. (1989), for the months of extreme SST: warmest in April (a–c), coldest in July (b–d).

ably with these observations (Schott 1986; Schott et al. 1988; Visbeck 1989; Visbeck and Schott 1992). The current meter measurements made between October 1984 and October 1986 in and below the Somali Current at the equator (Schott et al. 1989, 1990) are of particular importance to the present study of meridional heat transport. These unfortunately short time series suggest that only the upper 125 m or so of the Somali Current reverses direction with the monsoon, while the 125–500 m range flows northward year round. Weak currents were measured in the 500–1000 m range, but a conspicuous seasonal reversal was observed again at 3000 m, with 0.10 m s^{-1} to the northeast during the southwest monsoon and 0.07 m s^{-1} to the southwest during the northeast monsoon (i.e., a flow at 3000 m in the same direction as the surface Somali Current). Based on a comparison with other (nonsimultaneous) current meter measurements at 4°S and 5°N and with historical salinity and oxygen distributions near surfaces $\sigma_\theta = 25$ (mean depth 110 m), 26.6 (250 m), and 27.2 (675 m), these authors furthermore speculated that the flow in the 100–500 m range is continuously northward between 5°S and 5°N during the southwest monsoon but converges near 2°N during the northeast monsoon (northward flow between 5°S and 2°N, southward flow between 2°N and 10°N). The model behaves similarly, with important consequences for the seasonal cycle of heat transport, as shown below. More hydrographic sections were occupied in December 1986–January 1987 and in July–August 1987 in the same region. Salinity and oxygen distributions on $\theta = 1.8$°C (close to 3000 m where the deep current was observed to reverse the year before) did not confirm the flow reversal (Warren and Johnson 1992). The distributions suggested instead southwestward flow during both seasons. However, because the 1987 monsoon was extraordinarily weak, while there was nothing anomalous about the 1984–86 winds, we are inclined to consider Schott et al.'s observations as more relevant for a climatological study.

b. Heat budget

Figure 4 contrasts the model sea surface temperature (SST, upper panels) with the COADS[3] climatology [as plotted by Rao et al. (1989), lower panels] for the warmest (April, left panels) and coldest (July, right panels) months of the year. In both model and observed fields, warmest temperatures occur between 5°S and 15°N, and coldest temperatures are found along the

[3] Comprehensive Ocean–Atmosphere Data Set (Slutz et al. 1985).

western boundary. Position and seasonal migration of the thermal equator throughout the seasonal cycle, position, and time of occurrence of coastal upwellings also roughly agree when one compares the model with the observations. Warmest temperatures from the model at the 5-m level are, however, about 2°C too warm and cold temperatures are too cold. This is partly due to the fact that we are comparing an instantaneous nonaveraged model output to a smooth climatology. We must also note that there are large differences between climatologies. For instance, the July SST map from Hastenrath and Lamb's (1979) atlas compares better with Fig. 4b because it shows much colder water along the East African coast than Fig. 4d does, with a distribution very similar to Fig. 4b. It does not, however, show any temperature higher than 30°C as the model has simulated. That is certainly a consequence of our parameterization of radiation terms as constants,[4] as well as of the smoothness of the monthly winds, which yields underestimated mixing and evaporation.[5] This flaw also appeared in the simulations of the Atlantic and Pacific seasonal cycles (Philander and Pacanowski 1986a; Philander et al. 1987). It should be emphasized that shortcomings in the parameterization of diabatic processes are always exacerbated in sensitive parameters such as SST[6] and that presently developed coupled models also fail to simulate SST and its seasonal changes adequately (e.g., Mechoso et al. 1995). Of importance to our purpose is that warm and cold SST values occur at the right time of the year and, therefore, that the model ocean has mechanisms to warm and to cool the upper layers when it should.

Integrated vertically (in z) from bottom to surface and zonally (in x) from the western coast ($x = X_W$) to the eastern coast ($x = X_E$), the heat equation at a given latitude y can be written

$$\underset{(1)}{\frac{\partial}{\partial t}\langle \rho c_p \theta \rangle} + \underset{(2)}{\frac{\partial}{\partial y}\langle \rho c_p \theta v \rangle} = \underset{(3)}{\int Q_{\text{net}} dx} + \underset{(4)}{\text{diffusive terms}},$$

where $\langle\ \rangle$ stands for $\int\int (\ ) dx dz$. [Advective and diffusive fluxes vanish at the (stepwise straight) model boundaries because flow and temperature gradients are set to zero at the appropriate grid points.] Term (1) represents the rate of change of heat content, term (2) the divergence of meridional heat transport (Bryan 1962), term (3) the zonally integrated net surface heat flux into the ocean, and term (4) the divergence of lateral diffusive fluxes through the latitude under consideration.

The upper panels of Fig. 5 show the seasonal cycle of the zonally averaged net surface heat flux

$$\frac{1}{(X_B - X_W)} \int Q_{\text{net}} dx$$

(positive into the ocean) as a function of latitude, as reconstructed from the model output (panel a) and as estimated from data by Hsiung et al. (1989, panel b) and Hastenrath and Lamb (1980, panel c). In the model, solar radiation is constant so that the variation in Q_{net} is almost exclusively caused by variations in the latent heat flux, not a realistic simplification, see appendix A. Not unexpectedly then, there are many differences between Fig. 5a and Figs. 5b,c. For instance, the semiannual maximum of net incoming heat flux equatorward of 15°N is clearly stronger in February–April than in September–November in the observations (panels b and c), while it is of similar magnitude in these seasons in the model (panel a). Also, only in the model do the negative values of the Northern Hemisphere heat flux in January extend south of the equator and persist till April. There is no equivalent in the observations of the model isolated energy gain extremum in January–April near 10°S. Finally, amplitudes of the net surface heat flux in the model generally differ from the observations by more than the 20 to 30 W m^{-2} commonly accepted as the observational error bar. Without pretending to justify any of the model parameterizations leading to this situation, we must note, however, that larger than expected differences also exist between Figs. 5b and 5c: up to 90 W m^{-2} in the northern part of the basin, probably because of differences in resolution (the surface area of ocean becomes very small). Nevertheless the gross tendency for a net energy gain by each hemisphere during its own summer season exists in the simulation, as does the semiannual variation centered on 5°N, in particular the rapid transition from maximum heat gain in April–May to minimum heat gain in June–July.

The middle panels of Fig. 5 show in a similar fashion seasonal cycles of the zonally averaged rate of change of heat storage

$$\frac{1}{(X_B - X_W)} \frac{\partial}{\partial t} \langle \rho c_p \theta \rangle$$

as a function of latitude, as calculated from the model (panel d) and as estimated by Hsiung et al. (1989; panel e) and Hastenrath and Greischar (1993; panel f). Figure 5d was generated from the instantaneous monthly output by computing the top to bottom heat content at each latitude and longitude, averaging zonally and finite differencing in time. The result was averaged over 5° latitude, the same resolution as the

[4] Longwave radiation cannot limit SST growth if it is kept constant rather than following a σT^4-like law, and constant shortwave radiation misses the effect of spatial and temporal inhomogeneities in cloudiness.

[5] Parameterizations adopted to compensate for the lack of high-frequency wind fluctuations (see appendix A) may be insufficient.

[6] Mixed layer depth is another sensitive quantity that, in many locations, is poorly simulated by the model (recall the effect of the limited penetration of shortwave radiation in section 2a). This has discouraged previous researchers (Molinari 1990, personal communication) from further examination of this model's results. This was perhaps too severe a conclusion, as the rest of this paper will argue.

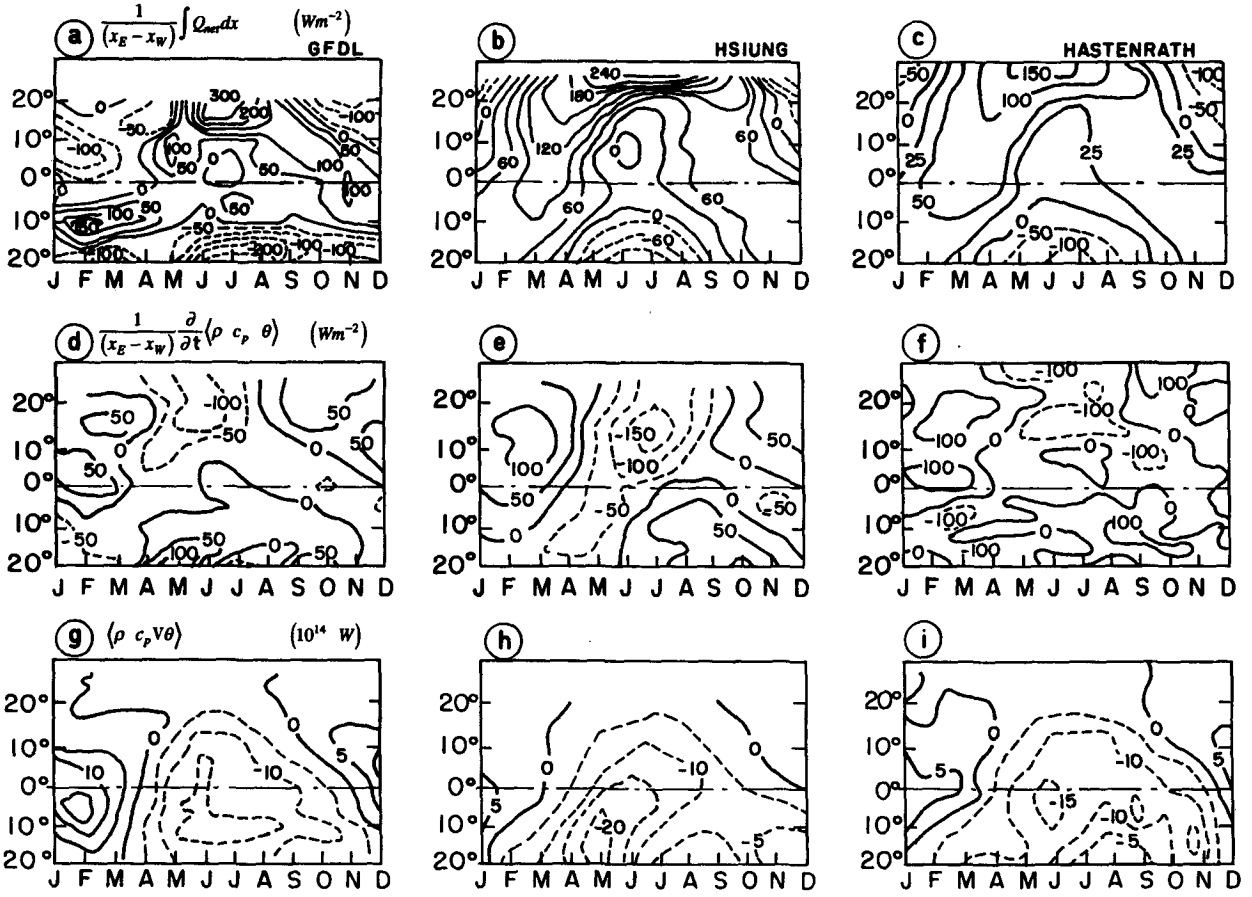

FIG. 5. Contrast between terms of the integrated heat budget from the model (left panels), from Hsiung et al.'s (1989) analysis (middle panels), and from Hastenrath and Lamb's (1980) (c) or Hastenrath and Greischar's (1993) (f–i) analyses (right panels). All terms are presented as a function of time and latitude. Upper panels (a–c) show the zonally averaged net heat flux into the ocean in W m^{-2}, middle panels (d–f) the zonally averaged rate of change of heat content in W m^{-2}, and lower panels (g–i) the net meridional heat transport in 10^{14} W (positive northward).

Hsiung et al. analysis. Figures 5e and 5f were generated by their authors in a similar fashion but using climatological oceanic data from only the upper 300 m and 400 m respectively, on the assumption that time variation below these levels contributed little to the time variation of total heat content (this assumption holds in the model). All figures [as well as a similar one by Levitus (1984)] display the largest increase in heat storage in boreal spring and its largest decrease in boreal summer. Amplitudes are of comparable magnitude, with those from the model being weaker overall.

The lower panels of Fig. 5 show the seasonal cycle of the net meridional heat transport as a function of latitude. Figure 5g was computed directly from the model monthly output, vertically and zonally integrating at each latitude the product $(\rho c_p \theta v)$.[7] [The model net diffusive heat flux through each latitude (not shown) was also computed; it exhibits little seasonal variation and its maximum value (0.15 pW), found at 5°S, is ten times weaker than the extrema of $\langle \rho c_p \theta v \rangle$.] Quantities plotted in Figs. 5h–i were obtained as residuals: neglecting the diffusive terms (4) in the heat equation, the divergence of heat transport (2) is the difference[8] between the net heat influx at the surface (3) and the rate of change of heat storage (1); integrating (2) southward from a closed northern wall assuming no Indonesian Throughflow yields $\langle \rho c_p \theta v \rangle$. Figure 5h appears smoother than Fig. 5i because it was drawn from the values published in Hsiung et al.'s Table 1 in order to obtain the same scales and contour interval (0.5 pW) as in Fig. 5g, while Fig. 5i was drawn after Hastenrath and Greischar's original figure (for a better comparison of the two observational estimates,

[7] ρc_p was kept constant at the value 4.33×10^6 J m^{-3} K^{-1} chosen by Hsiung et al. (1989).

[8] Unlike in the northern Atlantic and Pacific Oceans, this difference is between quantities of opposite sign, which adds confidence in the sign of the result, see section 4c.

see Hsiung et al.'s original figure as redrafted in Fig. 17i, keeping in mind that Hastenrath and Greischar and Hsiung et al. bound their domain at slightly different eastern longitudes).

General patterns roughly agree. In both hemispheres there is southward heat transport in boreal summer and northward transport in boreal winter (i.e., heat transport is toward the winter hemisphere year round). Quantitatively, the differences between the model and Hsiung et al. estimates (Figs. 5g–h) are no larger than those between the two observational estimates (Figs. 5h–i). The annual mean southward heat transport from the model (estimated by averaging the instantaneous monthly fields), however, has about half the amplitude of estimates based on data, as summarized in Fig. 6. This will be discussed further in section 4a. What does emerge from the analysis is that, although model and observational estimates of the circulation and of the various terms of the heat budget by no means agree in detail, their seasonal evolution has similar features, prompting a deeper investigation of the mechanisms in the model responsible for reversing the sign of the heat transport annually. It is worth mentioning that McCreary et al.'s (1993) $2\frac{1}{2}$-layer model, which includes thermodynamics (and considers seasonally varying radiation terms), simulates a seasonal cycle of heat transport very similar to the GFDL model one (McCreary 1994, personal communication).

As explained in appendix B, it is not possible at this stage to quantify the relative importance of the diabatic versus adiabatic components of heat transport introduced earlier. This issue is reconsidered in section 4d, where it will be shown that adiabatic processes seem to dominate the seasonal transport of heat for much of the time.

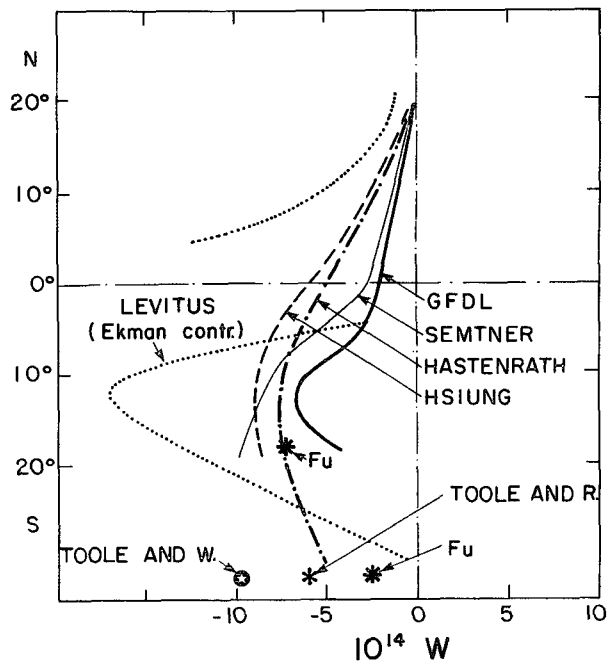

FIG. 6. Annual-mean meridional heat transport as a function of latitude from the model (curve labeled GFDL), from two air–sea fluxes climatologies (HASRENRATH: Hastenrath and Lamb 1980; HSIUNG: Hsiung et al. 1989), and from another realistic ocean model (SEMTNER: Meehl et al. 1982). Also plotted are the annual-mean Ekman contribution to the net heat transport (LEVITUS: Levitus 1987) and estimates of the divergence of heat transport from hydrographic sections (TOOLE AND R.: Toole and Raymer 1985; FU: Fu 1986; TOOLE AND W.: Toole and Warren 1993). Note that, for a better comparison with the model, for which the annual-mean results simply from an average of 12 values, the curve labeled HSIUNG was obtained by averaging the 12 monthly values quoted in her 1989 paper. That curve exhibits lower values than the annual-mean curve published by Hsiung (1985), which goes up to -8×10^{14} W at the equator and -15×10^{14} W at 20°S.

3. Mechanisms for the model meridional heat transport

Consider the simulated heat transport at, say, 5°N in August (Fig. 5g). As mass is conserved, a southward heat transport across that latitude implies that the transport-averaged temperature of the southward portion of the flow exceeds the transport-averaged temperature of the northward portion. (The opposite is true when the heat transport is to the north, as in February.) Our goal is to identify the warm and cold waters whose motion contributes most to the net heat transport.

The simplest circulation pattern yielding southward heat transport is one where the net southward flow is concentrated in the surface layers with compensating northward return flow below, at a lower temperature. As the decrease of temperature with depth is close to monotonic, the greater the vertical extent of the northward-flowing layer, the larger the temperature difference between southward and northward flows and the greater the southward heat transport. This kind of configuration is the basis of the Levitus (1987) work on the contribution of meridional Ekman transport to meridional heat transport in each oceanic basin. His result for the Indian Ocean (assuming no Indonesian Throughflow) is reproduced as Fig. 7a. Figure 7b presents an analogous calculation using, instead of the Levitus (1982) climatology, the GFDL model surface and depth-averaged temperatures (the computation is not made equatorward of about 2° latitude where Ekman dynamics break down). The close similarity between the two figures illustrates that the flaws in the model temperature structure have little effect on such integrated quantities.

What is interesting about Fig. 7a is that it exhibits the same seasonal pattern as Figs. 5h–i (with exaggerated amplitudes): northward heat transport north of 10°S during the northeast monsoon (boreal winter), southward heat transport during the southwest monsoon (boreal summer). Since the Ekman layer has, by construction, a warmer temperature than the return flow year-round, that seasonal pattern simply reflects the pattern of Ekman transport itself. Returning to Figs. 1a,b and Figs. 1e, f, this means that, north of 10°S dur-

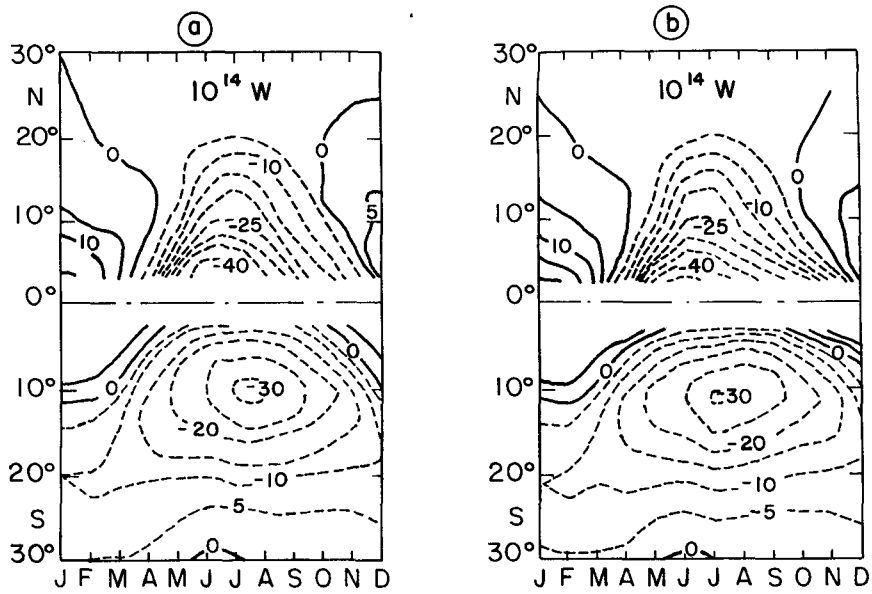

FIG. 7. Ekman contribution to the net meridional heat transport as a function of time and latitude, as redrawn from the Levitus (1987) publication (a) and as computed from the model (b). Contours are 5×10^{14} W.

ing both monsoon seasons, the near-equatorial change in direction of the zonal component of the wind drives a zonally integrated meridional Ekman transport that does not change sign as the equator is crossed.

Thus, the Indian Ocean has a powerful way to reverse the sign of its meridional heat transport throughout the year: reversing the sign of its surface mass transport in response to the wind reversals. The purpose of studying the GFDL simulation in more detail is to establish whether this is indeed the dominant mechanism. We must check whether the seasonally varying Ekman contribution is not dwarfed by another powerful vertical cell [as in the South Atlantic, e.g., Roemmich (1983)] or horizontal cell [as in the tropical Pacific, see Bryden et al. (1991)]. Ideally, we would also like to establish whether the Ekman circulation is involved in both components of the net heat transport or only in what we called its adiabatic component. In the following sections, we examine first (§3a) the contribution of the zonally integrated circulation, second (§3b) that of the non-zonally integrated circulation.[9]

a. *Relative contributions of the zonally integrated and of the vertically integrated circulations*

Let us split v and θ into zonally averaged and residual fields:

$$v = \tilde{v} + v'$$

$$\theta = \tilde{\theta} + \theta',$$

with, for example,

$$\tilde{v} = \frac{1}{X_B - X_W} \int v dx,$$

X_E, and X_W being respectively the eastern and western longitudes of the basin at the latitude considered. This yields for the net meridional heat transport:

$$\langle \rho c_p v\theta \rangle = \langle \rho c_p \tilde{v}\tilde{\theta} \rangle + \langle \rho c_p v'\theta' \rangle,$$

where $\langle\ \rangle$ stands for $\int\int (\ )\, dxdz$ as before. The contribution $\langle \rho c_p \tilde{v}\tilde{\theta} \rangle$ (Fig. 8a) can be thought of as the contribution of the zonally integrated circulation, that is, of a meridional cell, while the residual $\langle \rho c_p v'\theta' \rangle$ (Fig. 8b) can be attributed to a horizontal gyre and eddy fluxes. The contribution of the horizontal gyre can be identified with that of the vertically integrated circulation, and obtained by splitting v and θ into vertically averaged and residual fields (e.g., $v = \bar{v} + v''$; $\bar{v} = H^{-1} \int v dz$, with H the ocean depth at the longitude and latitude considered), yielding $\langle \rho c_p v\theta \rangle = \langle \rho c_p \bar{v}\bar{\theta} \rangle + \langle \rho c_p v''\theta'' \rangle$. The very close similarity between $\langle \rho c_p \bar{v}\bar{\theta} \rangle$ (not shown) and $\langle \rho c_p v'\theta' \rangle$ indicates that the contribution of the eddy fluxes to $\langle \rho c_p v'\theta' \rangle$ is negligible. Figure 8, therefore, illustrates the clear dominance of the meridional cell over the horizontal gyre (the same 0.5-pW contour was used on both figures).

The model vertically integrated circulation is represented in Fig. 9 by the horizontal streamfunction for February (panel a) and August (panel b), in parallel

[9] The analysis of the non-zonally integrated fields is actually the most informative. What is, however, more routinely computed in model analysis, and, thus, more readily found in the literature, are zonally integrated fields. Hence, the order of our presentation aimed at interpreting zonally integrated quantities in the light of non-zonally integrated ones.

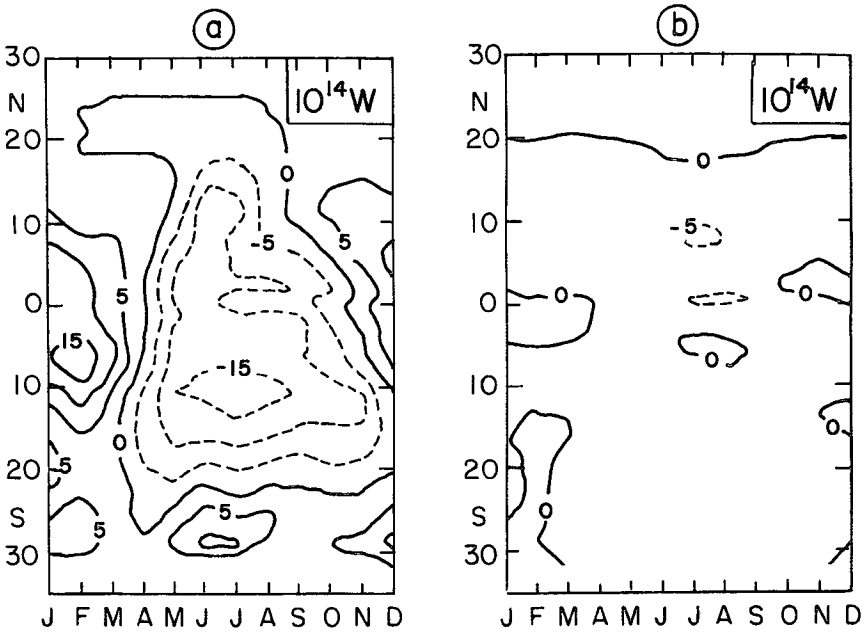

FIG. 8. Contribution to the net meridional model heat transport of (a) the overturning cell and (b) the residual. Fields are plotted as a function of time and latitude. Contours are 5×10^{14} W. The pattern in (a) is very close to the pattern of net heat transport (Fig. 5g), indicating the strong predominance of the overturning cell. The pattern in (b) closely resembles the pattern of the contribution of the depth-averaged horizontal circulation (not shown), which is thus negligible.

with the Sverdrup streamfunction deduced from the wind stress field assuming a quasi-steady state at each month (panels c and d). The model horizontal circulation is strong (maximum intensities of 34×10^6 $m^3 s^{-1}$ in February and 42×10^6 $m^3 s^{-1}$ in August) and very similar to the Sverdrup streamfunction. We will see later (section 4b) that the February pattern is actually partly dominated by the deep circulation. The August pattern, however, and the annual mean pattern (not shown) exhibit many of the features of the surface circulation. (In that respect, one can argue that the ability of the model to simulate known features of the surface circulation is more a test of the wind stress field used to force the model than of the model itself.) Differences between Figs. 9a and 9c, and between Figs. 9b and 9d, reflect the influence of model topography (note, e.g., the meridional deflection of isolines in the vicinity of the Chagos Laccadive Plateau at 75°E at and south of the equator) and the influence of advection (meridional displacement of the zero contour, intensification of the gyres). Such a horizontal circulation could contribute to heat transport if it was associated with large enough horizontal gradients of the depth-averaged temperature, which are themselves most often associated with topographic effects (shallower warmer boundary currents, deeper colder interior). The lesson from Fig. 8 was that those horizontal gradients are negligible compared to the vertical gradients associated with meridional overturning. February, when the relatively warm Somali Current flows southward, is in fact a month of northward heat transport and August, when the Somali Current flows northward, is a month of southward heat transport.

This last point is illustrated by Fig. 10. Figure 10a shows the seasonal cycle of the net meridional mass transport in the upper 165 m of the simulation[10] as a function of latitude. The seasonal pattern of the upper 165-m mass transport resembles the seasonal pattern of meridional heat transport (Figs. 5g or 8a): positive values in boreal winter, negative values in boreal summer. In boreal summer, a temperature difference of 16.5°C is needed between the southward-flowing upper layer and the underlying return flow at 5°S to recover the heat transport values of Fig. 5g. Around February, one would need a 37.5°C temperature difference, clearly an unrealistic value, which indicates that a more complicated circulation pattern exists at this time. Figures 10b,c show how the 0–165 m meridional mass transport is distributed horizontally in February (panel b)

[10] Fairly similar pictures are obtained if one considers the upper 100 m or the upper 250 m. The pictures are continuous across the equator (unlike the Ekman transport picture) as long as one integrates to a depth deeper than the vertical scale of the equatorial "roll" discussed later.

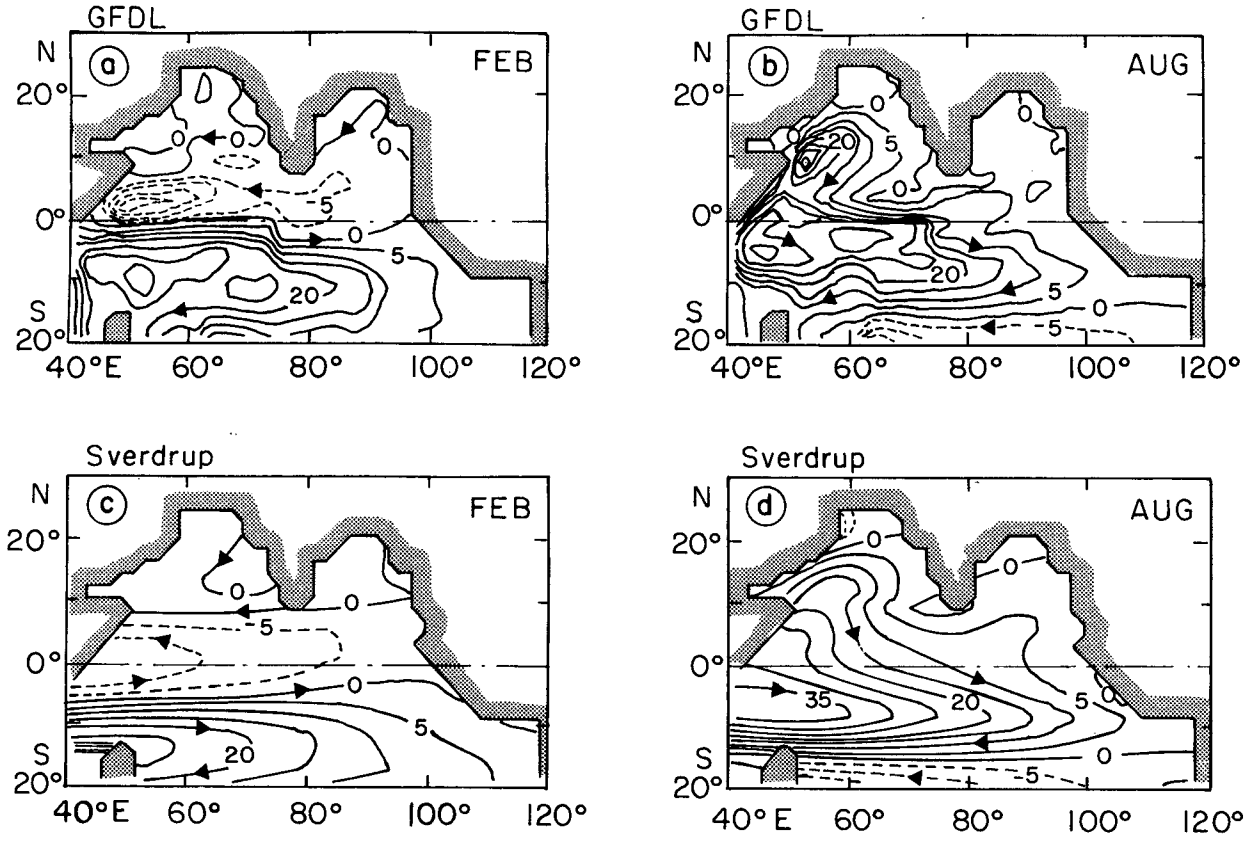

FIG. 9. Contrast between the model horizontal streamfunction (upper panels) and the Sverdrup streamfunction (lower panels) for the northeast monsoon (February, left) and the southwest monsoon (August, right). Contours are 5×10^6 m^3 s^{-1}. The Sverdrup streamfunction has been computed from the monthly wind stress curl assuming an equilibrium at each month, and the calculation was done continually across the equator, ignoring that the vorticity equation right at the equator is unlikely to be linear.

and in August (panel c). A net northward transport in the upper 165 m is obtained in February (Fig. 10a) because the northward interior part of the flow exceeds (in a zonally integrated sense) the southward Somali Current (Fig. 10b). This implies net downwelling across 165 m in the northern Indian Ocean, at a time when indeed the wind stress curl drives Ekman downwelling (Fig. 1c). Similarly, the 0–165 m net meridional mass transport in August (Fig. 10a) is dominated by a southward interior flow, despite a strong northward Somali Current (Fig. 10c). This implies upwelling from the lower into the upper layer, again consistent with a wind-driven circulation dominated (in a zonally integrated sense) by Ekman upwelling (Fig. 1d).

We now consider the meridional circulation in more detail. The meridional streamfunction is drawn in Fig. 11 for February (left) and August (right). Figures 11a–d present it as a function of depth for the upper 500 m (upper panels) and for the whole water column (middle panels). Figures 11e–f present it for the whole water column as a function of potential temperature. To generate these last two plots, the field of meridional velocity was first binned into temperature classes, then integrated zonally and vertically between two isotherms.[11] Note that the amplitudes of the meridional cells have the same order of magnitude as the amplitudes of the horizontal gyres (Fig. 9), but that they are associated with large temperature differences (of order 15°C in August as anticipated above). What is most striking in Fig. 11 is the difference between the circulations depicted for February and August.

In August (Fig. 11f), the zonally integrated flow north of 5°S collapses into a simple 15×10^6 m^3 s^{-1} meridional cell formed of northward motion in the 10°–15°C temperature range, upwelling north of 10°N and southward motion near the surface at about 27.5°C. The associated heat transport is about 0.9 pW. South of 5°S, the cell is strengthened by an additional 10×10^6 m^3 s^{-1} flowing in at about 17.5°C, upwelling in the 5°–10°S range and flowing out at about 25°C. This causes

[11] The streamfunction $\Psi(y, z)$ (Figs. 11a–d) results from $\int_z^0 \int_{X_W}^{X_E} \times v_{z'=cst} dxdz'$ [or, equivalently, from $-\int_y^{Y_N} \int_{X_W}^{X_E} w_{z=cst} dxdy'$]. By contrast, $\Psi(y, \theta)$ (Figs. 11e–f) results from $\int_\theta^{35°C} \int_{X_W}^{X_E} (\partial z/\partial\theta) v_{\theta'=cst} dxd\theta'$.

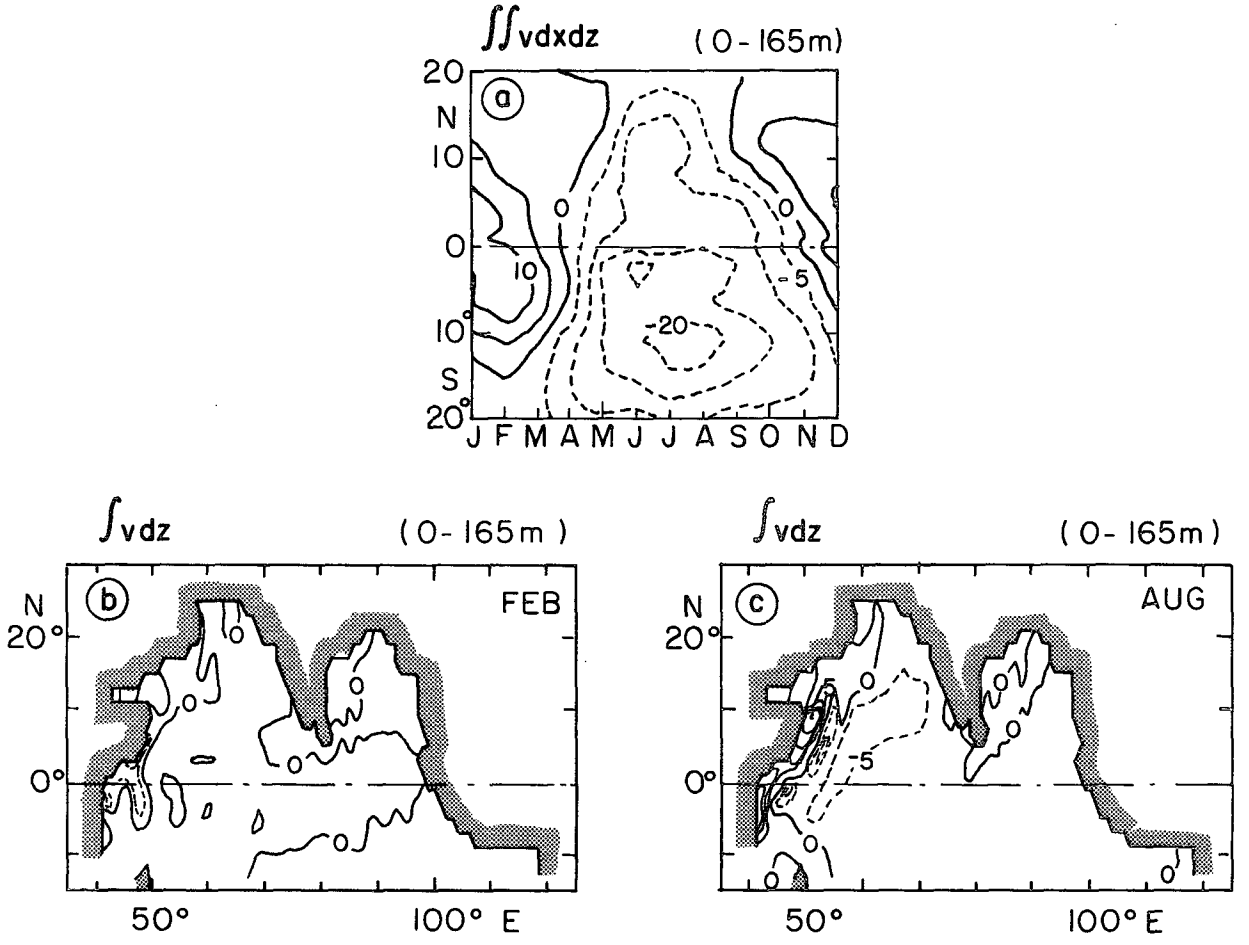

FIG. 10. The upper panel (a) shows the net meridional volume transport in the upper 165 m of the model as a function of time and latitude (contours of 5×10^6 m^3 s^{-1}). Note the similarity of pattern with the net heat transport (Fig. 5g). The lower panels show the horizontal distribution of the 0–165 m meridional transport during the northeast monsoon (Feb, left) and during the southwest monsoon (Aug, right). Contour interval is 25 m^2 s^{-1} for the positive values and 10 m^2 s^{-1} for the negative values. In both seasons, interior values dominate the zonal integral despite strong opposite values in the downwind upper Somali Current.

an additional heat transport of about 0.3 pW. This simple description adequately accounts for the heat transport values computed directly for August (Fig. 5g), it supports inferences drawn from Fig. 10, and regions of upwelling and southward flow respectively correspond to regions of Ekman suction and southward Ekman transport (Figs. 1d,f).

In February, the zonally integrated flow is not simply the reverse of the August cell. As in August, the flow in the 10°–15°C range (Fig. 11e) is to the north, but with smaller penetration into the Northern Hemisphere, and there is again upwelling near 10°S (consistent with Ekman suction, Fig. 1c). There is also evidence for a subcell south of 10°S returning surface water southward as in August, although much weaker (consistent with weaker values of southward Ekman transport in the 15°–10°S band, Fig. 1e). The striking difference between Figs. 11e and 11f is in the behavior of the northward 10°–15°C flow north of 10°S. A 5×10^6 m^3 s^{-1} fraction of the water upwelled near 10°S appears to flow northward at the surface, reaching 10°N where it downwells. This is consistent with the pattern of northward Ekman transport on both sides of the equator displayed on Fig. 1e and with the predominance of Ekman pumping in the 5°–10°N latitude band (Fig. 1c). What is surprising is the depth at which this water appears (in a zonally integrated sense) to downwell. It does not return southward in the 10°–15°C range where net northward flow is obtained. Rather it downwells even deeper along with the 10°–15°C water in the 5°S–5°N band to return as bottom water. In terms of net meridional heat transport, the northward 5×10^6 m^3 s^{-1} of 27.5°C surface water returning at 2.5°C contributes about 0.5 pW and the 15×10^6 m^3 s^{-1} of 12.5°C water returning at 2.5°C contributes about 0.6 pW. This accounts for the values computed directly for February (Fig. 5g) and illustrates the deficiencies of the simpler circulation pattern underlying the discussion of Fig. 10.

Figure 11, however, raises new questions. We must explain the large vertical scale of the February over-

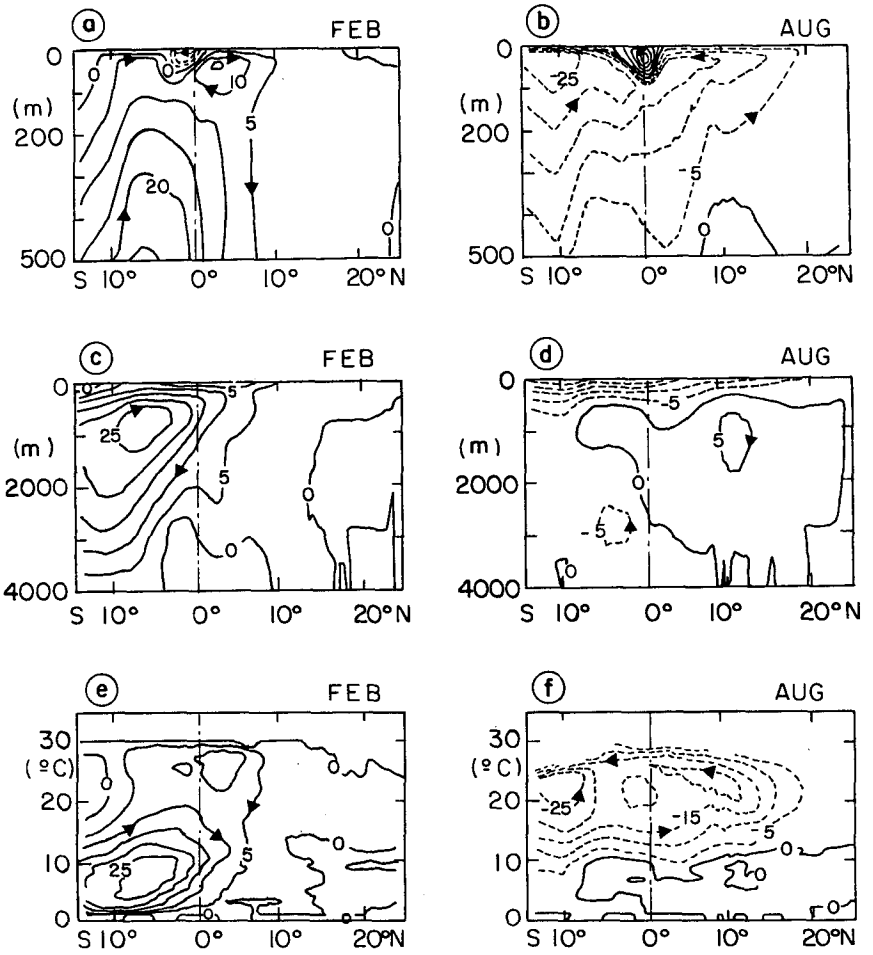

FIG. 11. Model meridional streamfunction for the northeast monsoon (Feb, left) and the southwest monsoon (Aug, right). The middle panels (c–d) represent the streamfunction as a function of latitude and depth over the whole water column, the upper panels (a–b) are a blown-up of the middle ones for the upper 500 m. (e–f) The streamfunction as a function of latitude and potential temperature. Contours are 5×10^6 m^3 s^{-1}.

turning cell in terms of the non-zonally integrated meridional circulation. We will emphasize in section 3b that streamlines should not be interpreted as individual fluid parcel trajectories (consistency with Fig. 11c does not require individual water parcels to move far at all) and in section 4d that streamlines can cross isotherms even in the absence of cross-isotherm fluxes. We must also discuss the large seasonal variations in the bottom circulation, which were unexpected, and we must comment on the equator-crossing of the surface layers, which involves in each season a shallow downwind cell opposing the surface branch of the main cell.

b. *Seasonal variation of the non-zonally integrated meridional circulation*

The most convincing way to investigate which components of the flow carry most of the heat seasonally would be to trace the motion of particles released in given temperature ranges. This may be attempted in a future run but could not be considered here given the once-monthly output of the present run. The tentative picture of the seasonally varying three-dimensional (3D) circulation that we are presenting results from studying various monthly snapshots of the horizontal and vertical flow.

According to Fig. 11, a first-order picture can be obtained by considering the horizontal circulation of three layers: a 0–100 m "surface" layer (temperatures higher than 20°C) within which, in a zonally integrated sense, water north of 10°S flows northward in February and southward in August; a 100–800 m "intermediate" layer (10°–20°C range) within which net transport is northward year-round and an 800 m–bottom "deep" layer (temperatures lower than 10°C) within which as much as 25×10^6 m^3 s^{-1} flow southward in February while there is no significant net flow in August. With this approach, the main features of the 3D

circulation causing the cross-equatorial heat transport can be summarized schematically as follows. During the northeast monsoon (left side of Fig. 12), 15×10^6 m^3 s^{-1} of northward surface interior flow at 27.5°C compensated by a southward transport in deep western boundary currents at about 5°C cause a 1.3 pW northward heat transport. This value is slightly tempered by a minor western boundary current subsystem of 5×10^6 m^3 s^{-1} of southward surface flow at 27.5°C with northward return at intermediate levels at about 12.5°C, causing a 0.3 pW southward heat transport [in agreement with an observational estimate by Schott et al. (1990)]. That brings the total transport to 1 pW to the north. During the southwest monsoon (right side of Fig. 12), 30×10^6 m^3 s^{-1} of southward surface interior flow at 27.5°C is compensated by flow in the western boundary current, in part (10×10^6 m^3 s^{-1}) at the surface, that is, at the same temperature (no contribution to the heat transport), in part (20×10^6 m^3 s^{-1}) at intermediate levels, causing 1.2 pW of southward heat transport. Details are given below, first for the simpler August pattern, then for the February one.

Consider Fig. 13 for August. The upper panels (a) show the surface layer, the middle panels (b) the intermediate layer, and the lower panels (c) the deep layer. The left panels, based upon vector plots of the transport per unit width, present schematics of the horizontal circulation vertically integrated over each layer. The right panels present the meridional component of that transport per unit width accumulated from the western boundary eastward at 5°N, 0°, and 5°S. Significant meridional flow occurs where significant zonal gradients of the accumulated transport are displayed. Values printed at 100°E represent the net meridional transport (i.e., the vertically and zonally integrated meridional velocity) through each layer at the latitudes chosen (values are rounded to the closest multiple of 5×10^6 m^3 s^{-1}). At a given latitude, the sum of these values over the three layers is necessarily zero (e.g., the sum, at 5°S, of -20×10^6 m^3 s^{-1} in the upper layer, $+25 \times 10^6$ m^3 s^{-1} in the intermediate layer, and -5×10^6 m^3 s^{-1} in the deep layer). Consider the incoming intermediate flow. According to Fig. 13b, it occurs essentially along the western boundary. The amount of water upwelled north of 5°N to return southward as surface water is of order 15×10^6 m^3 s^{-1}. A large fraction of the upwelling through 100 m occurs along East Africa (part of which is offset by downwelling on the offshore side of the wind jet), a non-negligible fraction occurs east of 65°E. At 5°N the southward surface flow (Fig. 13a) is the interior part of an anticyclonic gyre over the Arabian Sea (the contribution of the Bay

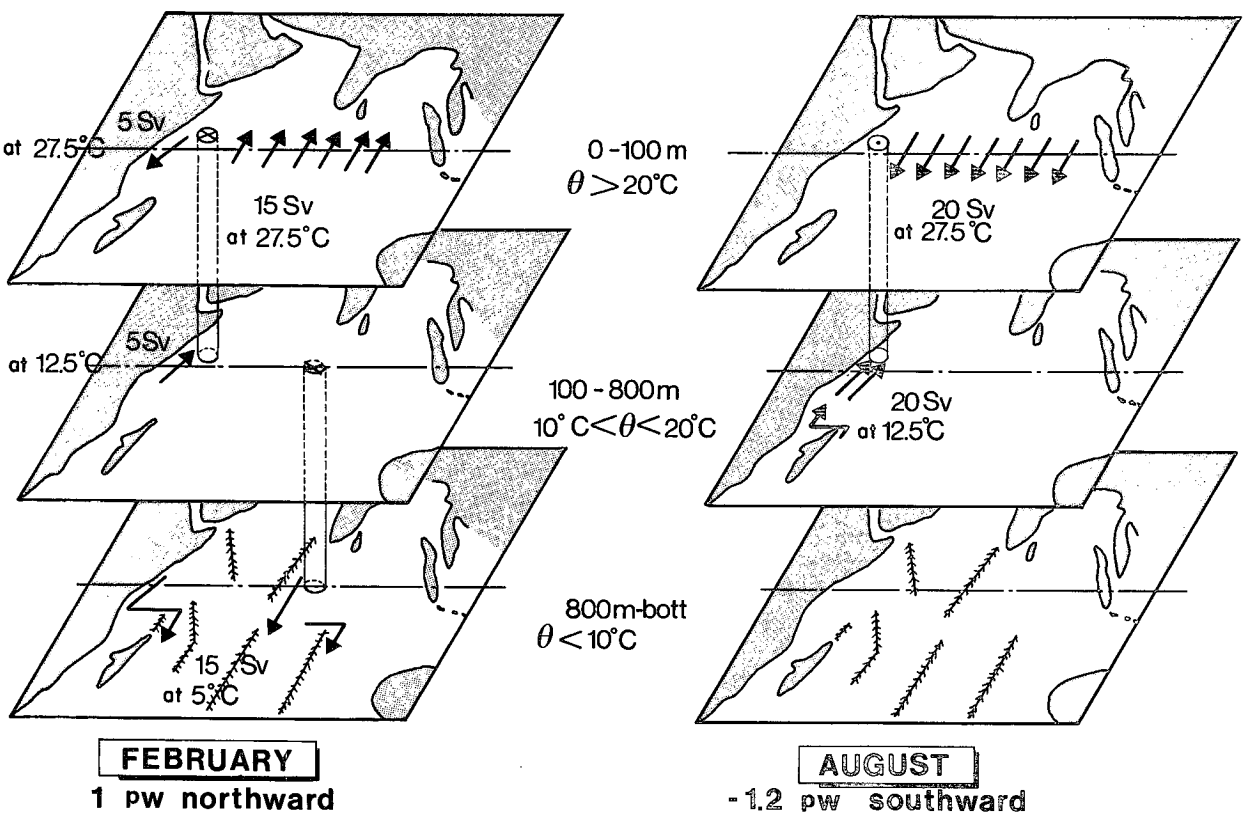

FIG. 12. Schematics of the components of the model's three-dimensional circulation contributing most to the net meridional heat transport during the northeast monsoon (Feb, left) and the southwest monsoon (Aug, right).

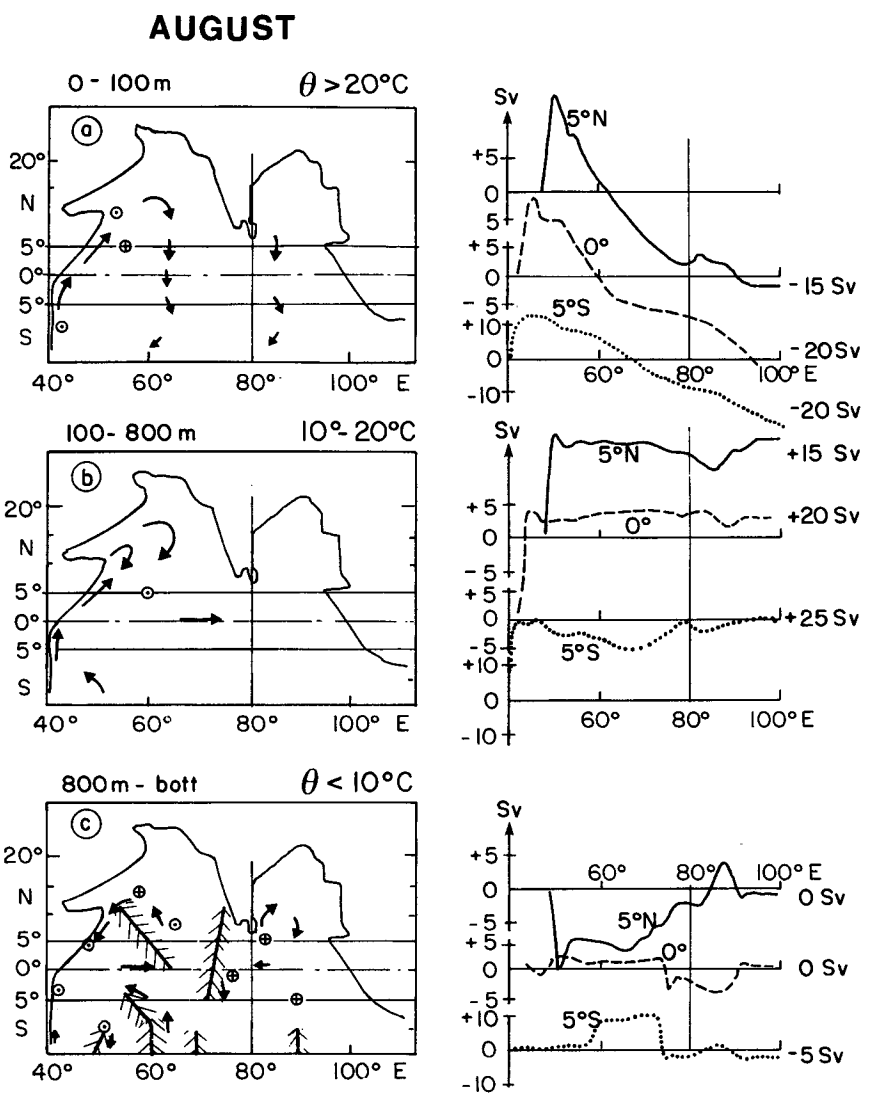

FIG. 13. Horizontal circulation in the upper (0–100 m, $\theta > 20$°C), intermediate (100–800 m, 10°C $< \theta <$ 20°C), and deep (800 m–bottom, $\theta <$ 10°C) model layers during the southwest monsoon (Aug). Left panels show schematics of the circulation integrated over the various layers, including indications of the vertical circulation *within* each layer (circles with dots mean upwelling, with crosses downwelling). The location of ridges is indicated for the deep layer. The right panels show the meridional velocity integrated over each layer and *accumulated* from the western boundary eastwards (in 10^6 m^3 s^{-1}) for three latitudes: 5°N, 0°, and 5°S.

of Bengal is negligible by comparison). Southward surface flow occurs throughout the interior at the equator and at 5°S as well. The actual crossing of the equator within the 0–100 m layer is discussed later. Very little exchange with the deep layer takes place. Most of the deep flow south of 2.5°N (Fig. 13c) occurs along the equator and the eastern flank of topographic features, a sign that, even if some adjustment is still taking place, the stratification imposed initially was at least not incompatible with the model topography and with the forcing applied continuously afterward. North of 2.5°N, the deep interior is also in motion, the main feature being a cyclonic gyre of order 10×10^6 m^3 s^{-1} in the southern Arabian Sea. The associated meridional motion reflects the pattern of vertical velocity through 800 m: downwelling (compressing the deep layer) in the west and upwelling (stretching it) in the east of the Arabian Sea, in qualitative agreement with quasi-steady linear vorticity dynamics.

Figure 14 is the equivalent of Fig. 13 for February. Consider again the incoming intermediate flow (Fig. 14b). Through 5°S, it amounts to about 20×10^6 m^3 s^{-1} and is concentrated at the western boundary. None of it reaches far into the northern Indian Ocean as it veers eastward along the equator after some overshooting. During this eastward motion 15×10^6 m^3 s^{-1}

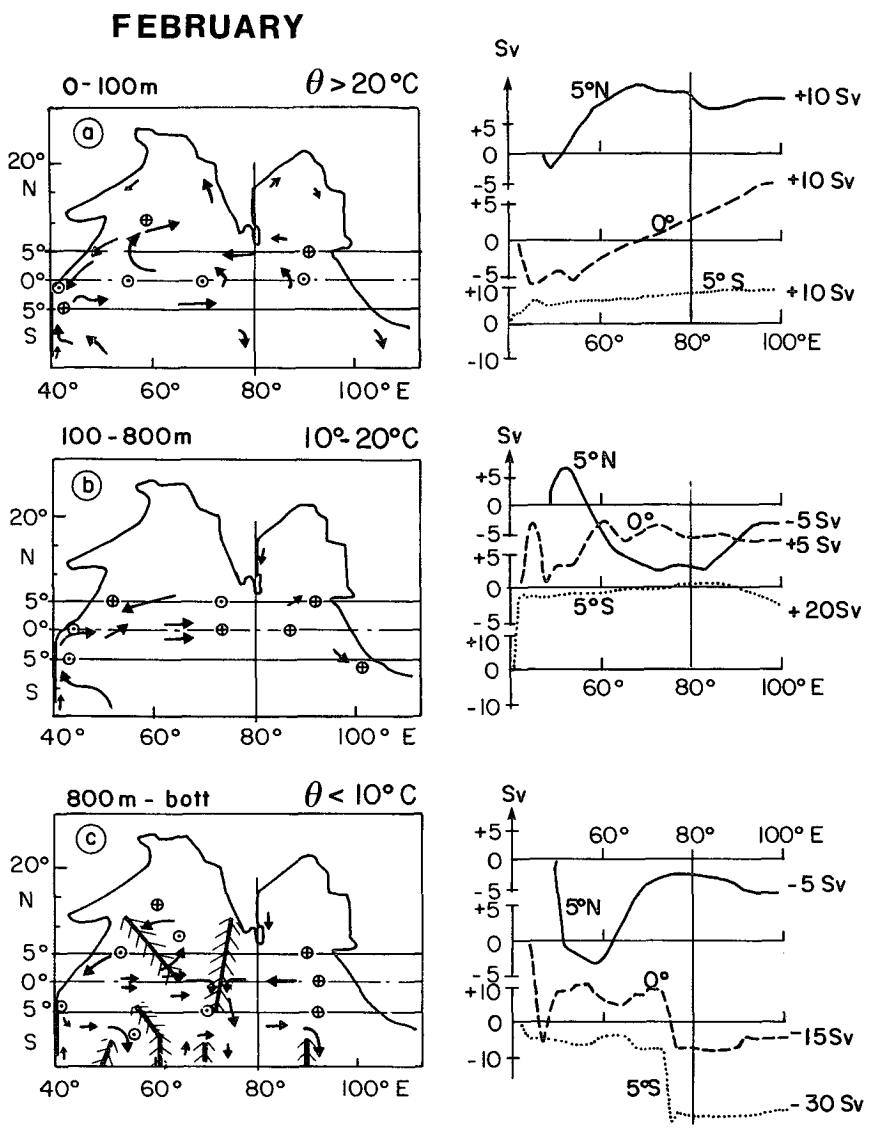

FIG. 14. Same as Fig. 13 but for the northeast monsoon (Feb).

downwell into the deep layer (Fig. 14c) and exit via southward boundary currents along topographic features (75°E at 5°S, 90°E at 10°S). The 10×10^6 m^3 s^{-1} of surface flow (Fig. 14a) crossing the equator over the whole interior (see details in the following paragraph) and crossing 5°N mostly west of 80°E are the same 10×10^6 m^3 s^{-1} of surface water crossing 5°S partly at the western boundary, partly in the interior[12] west of 80°E. Downwelling of this northward surface flow into the intermediate layer north of the equator occurs in the Arabian Sea, mostly west of 65°E and south of 10°N. The intermediate layer carries it back southwestward (Fig. 14b), most of it joining the eastward flow along the equator and adopting the same path as described above: downwelling along the equator, southward exit at 75°E (Fig. 14c). A smaller fraction downwells into the deep layer near the western boundary and exits along the western boundary of various topographic features (e.g., east of Madagascar). Thus, the lower cell dominating the zonal integral in Fig. 11e consists of a 3D flow confined along the western boundaries and the

[12] The way this surface flow is fed by upwelling from the intermediate layer is not as straightforward as suggested by Fig. 11e. The upwelling, which dominates the zonal integral near 10°S, occurs over the interior east of Madagascar and mostly feeds a southward surface flow (which, at 10°S, does not dominate the zonal integral). That flow eventually becomes the South Equatorial Current farther south, which feeds the northward boundary current east of Madagascar and the eastward South Equatorial Countercurrent near 2.5°S–5°S, hence ultimately feeding the surface northward flow under consideration.

equator. Superimposed on the deep pattern described above is a recirculating cyclonic gyre of order 15×10^6 $m^3 s^{-1}$ in the southern Arabian Sea, qualitatively consistent with the pattern of vertical velocity through 800 m as in August. This description illustrates the misleading character of figures such as Fig. 11e when interpreted as trajectories: nowhere is water sinking 3000 m abruptly. In section 4d, we will see more precisely where vertical motion occurs. Figure 21 for instance will reveal that the 20×10^6 $m^3 s^{-1}$, which cross the 5°C isotherm surface between 5°S and 5°N, occur over 40° longitude—that is, at a local velocity of 4×10^{-6} $m s^{-1}$—corresponding, in terms of vertical displacement, to the very modest value of about 10 m mo^{-1}.

Before discussing these seasonal variations further, let us reconsider Figs. 11a,b and comment on the way the model surface flow crosses the equator. In both seasons, the surface limb of the large cross-equatorial cell is depressed by a shallow cell of opposite direction straddling the equator. In terms of the non-zonally integrated circulation, this corresponds to a basinwide "roll" of downwind surface flow and upwind subsurface flow above 75 m (at lower levels, the crossing of the equator occurs along topography rather than in the ocean interior). Dynamically the surface branch is the frictional response (in the equatorial band where Ekman dynamics fail) to the cross-equatorial wind stress component. That causes upwelling on the upwind side of the equator, downwelling on the downwind side, and a meridional pressure gradient in between, confined meridionally within an equatorial radius of deformation and vertically within the equatorial thermocline. The subsurface branch flows down that pressure gradient (e.g., Cane 1979; Philander and Pacanowski 1980). If these equatorial cells were associated with any vertical temperature difference, they would lower the value of the cross-equatorial heat transport associated with the large cells because they flow in the opposite direction. The fact that they do not appear in Figs. 11e,f indicates that they simply recirculate water of homogeneous temperature and play no part in the heat budget.

4. Discussion

We now need to discuss how much of the model behavior is likely to apply to the Indian Ocean itself. By construction, the way the simulation transports heat is compatible with Levitus climatology and with Hellerman and Rosenstein wind stresses. Flaws in those fields can cause flaws in the model behavior. Seasonal variations in heat transport were found to agree qualitatively with indirect estimates based on surface heat fluxes and heat content variations; the robustness of which must be addressed. In the model, these variations could be traced to expected changes in the direction of the surface flow, however somewhat unexpectedly balanced by changes in the direction of the deepest flows. This needs further elaboration. We would also like to assess the role of diabatic processes in the heat transport reversals. Finally, we will comment on the impact on the heat transport of having blocked the Indonesian Throughflow in the model.

Concerning the 75-m deep rolls below which surface water crosses the equator in the model, we can simply mention that, although they are present in other numerical simulations with cross-equatorial winds and although they are dynamically understood; we are not aware of any observations confirming their existence in the real world.

a. Annual mean

Consider first the model annual-mean meridional streamfunction (Fig. 15), estimated by averaging the 12 monthly snapshots available. It is dominated by the southwest monsoon circulation, showing north of 15°S a net zonally integrated southward flow at the surface, northward flow in the 50–800 m range, and mostly southward flow below. This contrasts sharply with Toole and Warren's (1993) analysis at 32°S, which shows a net zonally integrated northward flow of 27×10^6 $m^3 s^{-1}$ below 2000 dbar and southward flow above (see also Warren 1994). If the circulation modeled at 15°S is to resemble more closely the circulation inferred at 32°S from observations, the model is missing some northward deep flow (and the shallower flow balancing it) on the annual mean. This is not unlikely, given the relatively shallow model ocean bottom and the smooth climatological stratification to which deep currents must adjust (appendix A). Moreover, the model deep overturning cell may be the result of ill-parameterized diffusion, as discussed in section 4d. Adding onto Fig. 15c a cell of 15×10^6 $m^3 s^{-1}$ of northward flow below 2000 m ($\theta \approx 2$°C) returning in the 200–1000 m range ($\theta \approx 15$°C) would cancel the deep overturning cell, offset the northward branch of the shallower cell, and add 0.8 pW to the model mean southward heat transport, bringing it closer to other observational estimates (Fig. 6). One must, however, keep in mind that the Toole and Warren analysis itself may need revisions: the large upwelling through 2000 dbars that it implies appears not to be supported by independent tracer measurements (Toggweiler 1993, personal communication).

b. Deep seasonal reversals

Adjusting the model circulation to accommodate a larger annual-mean heat transport will not, however, change the amplitude of its seasonal variation, and, in particular, that variations in deep currents are involved. As an illustration, notice that, on Figs. 9a,b, the August pattern of horizontal streamfunction is dominated by the surface circulation (Fig. 13a) while the February pattern (at least the conspicuous cyclonic gyre north of the equator) is dominated by the deep circulation (Fig. 14c). Whether or not this is realistic is a particularly difficult question to answer in view of the paucity of

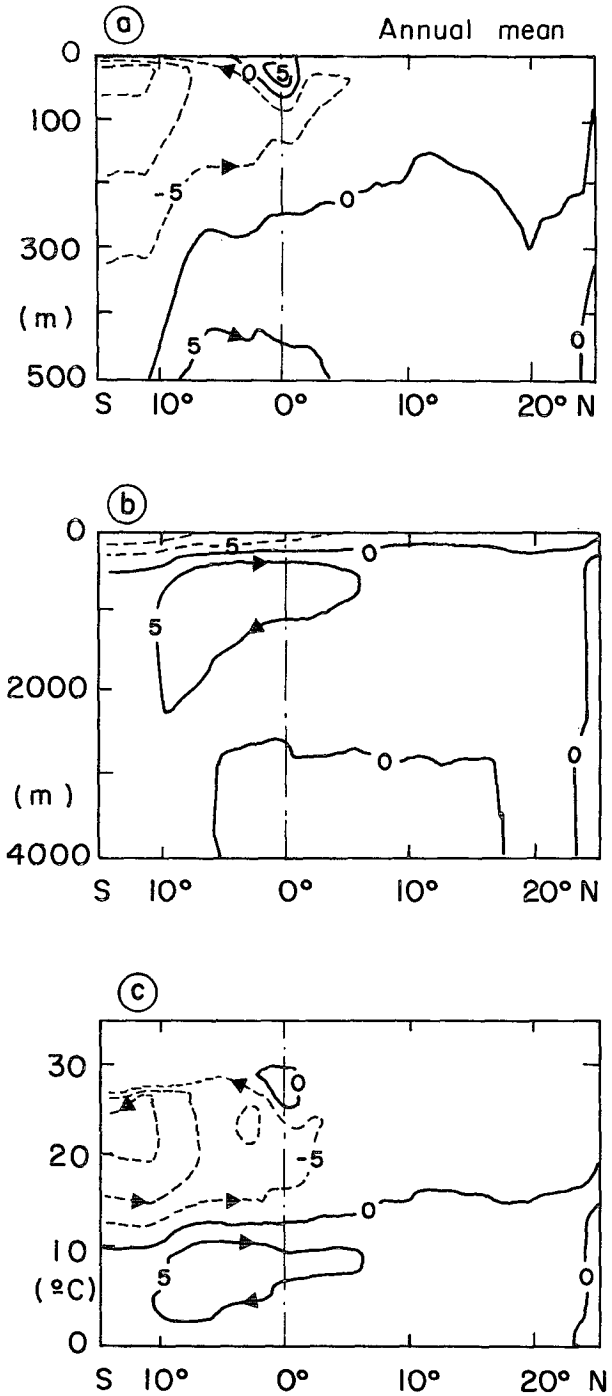

FIG. 15. Model meridional streamfunction for the annual mean (obtained by averaging 12 monthly values) as a function of latitude and depth over the upper 500 m (a), over the whole water column (b), and as a function of latitude and potential temperature (c). Contours are 5×10^6 m^3 s^{-1}.

relevant measurements. In the northern Arabian Sea (north of 8°N to separate it from the Bay of Bengal) most of the seasonal variations are confined to the upper 800 m, with Ekman-driven seasonal reversals of the basinwide shallow (warm) surface layer balanced by seasonal reversals of the thicker (cooler) western boundary current (see Fig. 16, in conjunction with Fig. 10). Farther south, however, variations in the deep flow occur because the intermediate layers of the boundary current keep flowing to the north year round. Thus, in the 0°–10°N region west of 80°E in February, surface water converging from the south across the equator and from the east from the Monsoon Drift Current downwells to intermediate levels, where further convergence with the still northward cross-equatorial boundary current causes downwelling into deeper levels. The credibility of that downwelling into the deep layers is therefore linked to the credibility of the convergences at the surface and intermediate levels. In view of Figs. 3a–c, we believe that the February surface circulation is realistic in the model. We also believe that the pattern of Ekman downwelling associated with the northeast monsoon season (Fig. 1c) is robust (different climatologies yield wind stress curl patterns that may disagree in amplitude but that agree in sign). Thus, the surface convergence seems to be a reality. The crucial observational fact supporting the model prediction is that, at the equator, only the upper 150 m of the otherwise northward Somali Current switch direction in response to the annual switch of the monsoons (section 2a), thus, supporting the reality of subsurface convergence as well. Furthermore, one-year long current measurements at 3000 m at the equator exhibited an annual reversal. That the deep circulation should experience seasonal variations may therefore be a reality too. Extrapolating details of the model behavior into a prediction for the real ocean is, however, difficult with the present run, given the short spinup and the subsequent uncertainties in the degree of adjustment of the deep layers. More numerical experiments (with a more recent model version) will be needed. Note that similar seasonal stirrings of deep western boundary currents suggestive of barotropic adjustment occur in the Pacific portion of Semtner and Chervin's model (Wilkin et al. 1995) and in Böning and Herrmann's (1994) simulation of the Atlantic.

c. *Indirect estimates of the seasonal heat transport*

We have also seen that the model exhibits a seasonal cycle of heat transport similar to that of Hsiung et al. (1989) or of Hastenrath and Greischar (1993). How much this should increase our confidence in the model behavior depends on how much confidence we should put in these indirect estimates. Figure 17 [after Hsiung et al. (1989)] presents in parallel for the three oceans and as a function of latitude the seasonal cycles of terms (1) and (3)[13] of the heat budget (in W m^{-2}), and of the resulting meridional heat transport (in 0.1 pW)

[13] See section 2b.

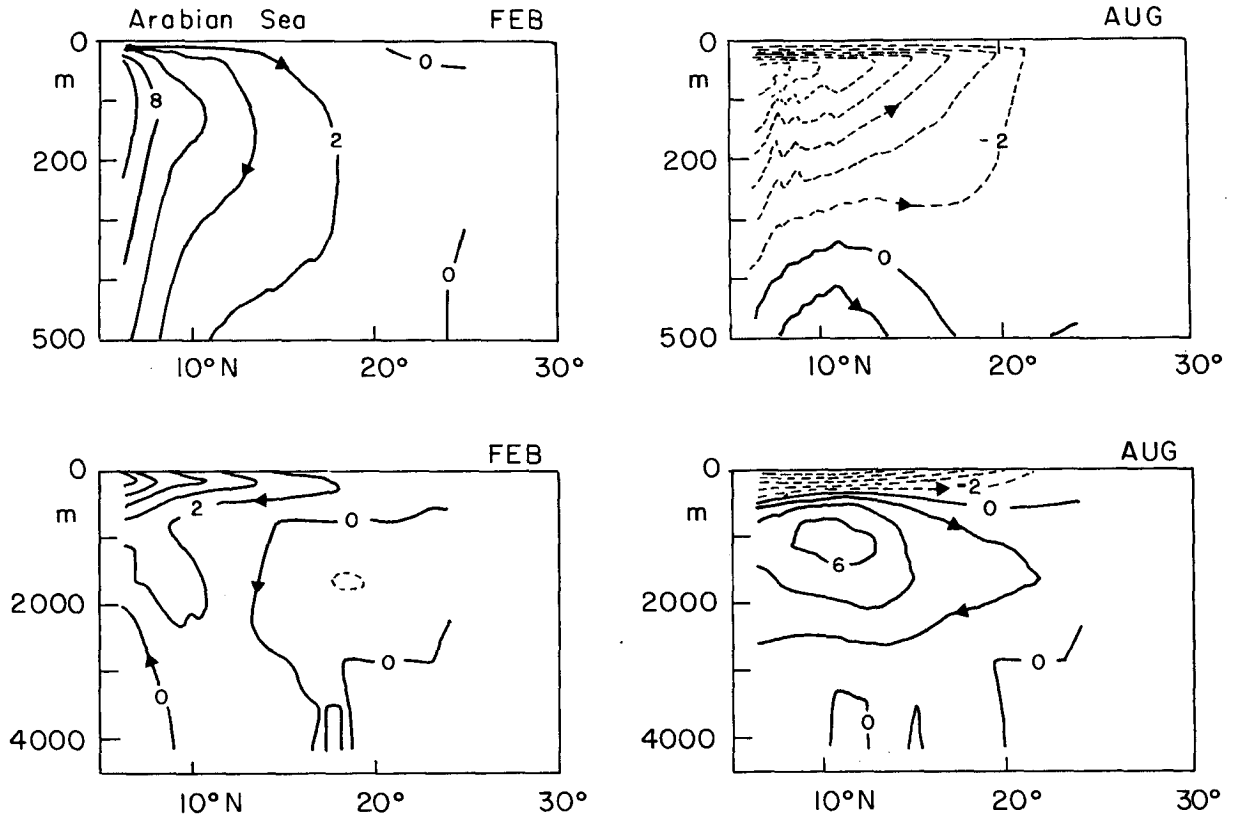

FIG. 16. Model meridional streamfunction (as a function of latitude and depth) for the Arabian Sea during the northeast monsoon (Feb, left) and the southwest monsoon (Aug, right). Upper panels show the upper 500 m and lower panels the whole water column. Contours are 2×10^6 m^3 s^{-1}.

obtained by integrating their difference from a northern boundary southward, assuming lateral boundaries closed. Consider first the Atlantic Ocean (upper panels) and the Pacific Ocean (middle panels). Except near the equator, rate of change of heat storage (Figs. 17a–d) and net heat flux into the ocean through the surface (Figs. 17b–e) are typically two large terms of identical sign whose difference constitutes the residual to be integrated meridionally. Any systematic error on one of those terms may result in an error in the sign of the residual that gets carried to lower latitudes during the integration, increasing with distance away from the northern boundary. Furthermore the horizontal 5° × 5° resolution with which terms (1) and (3) are being estimated is low compared to observed meridional gradients of oceanic properties in the Tropics. This is probably why simulations of the tropical Atlantic (Philander and Pacanowski 1986b; Böning et al. 1994) can exhibit patterns of heat transport as a function of month and latitude that agree with the indirect estimates far enough north of the equator but disagree more and more as the equator is approached. Near the equator, Fig. 17c shows a continuation of the higher latitude pattern in the northern Atlantic: a northward transport that is lower (ultimately reversing) in winter, higher in summer. Model studies exhibit an opposite cycle, with storage and release of heat between adjacent latitude bands yielding minimum northward heat transport in boreal summer. Model and indirect estimate are in better agreement in the tropical Pacific (Philander et al. 1987) where both predict a heat transport toward the winter hemisphere (northward in boreal winter, southward in boreal summer, Fig. 17f).

The uncertainty is much less in the Indian Ocean because, except between the monsoons, terms (1) and (3) (Figs. 17g–h) are of opposite sign. Their difference becomes the sum of large quantities of identical sign, with the sign of the sum much less likely to change even if errors contaminate either of the terms. Furthermore the latitude range over which the meridional integral is performed is much less than in the Atlantic and Pacific case, minimizing the danger of accumulating systematic errors. Our conclusion is that the pattern of heat transport toward the winter hemisphere exhibited by the indirect estimates (Figs. 17i, 5i) not only near the equator but in both hemispheres, is reliable and that the model's qualitative agreement with this pattern (Fig. 5g) is meaningful. Indirectly this adds confidence in the model prediction of deep layers stirring, for the following reason. According to Hastenrath

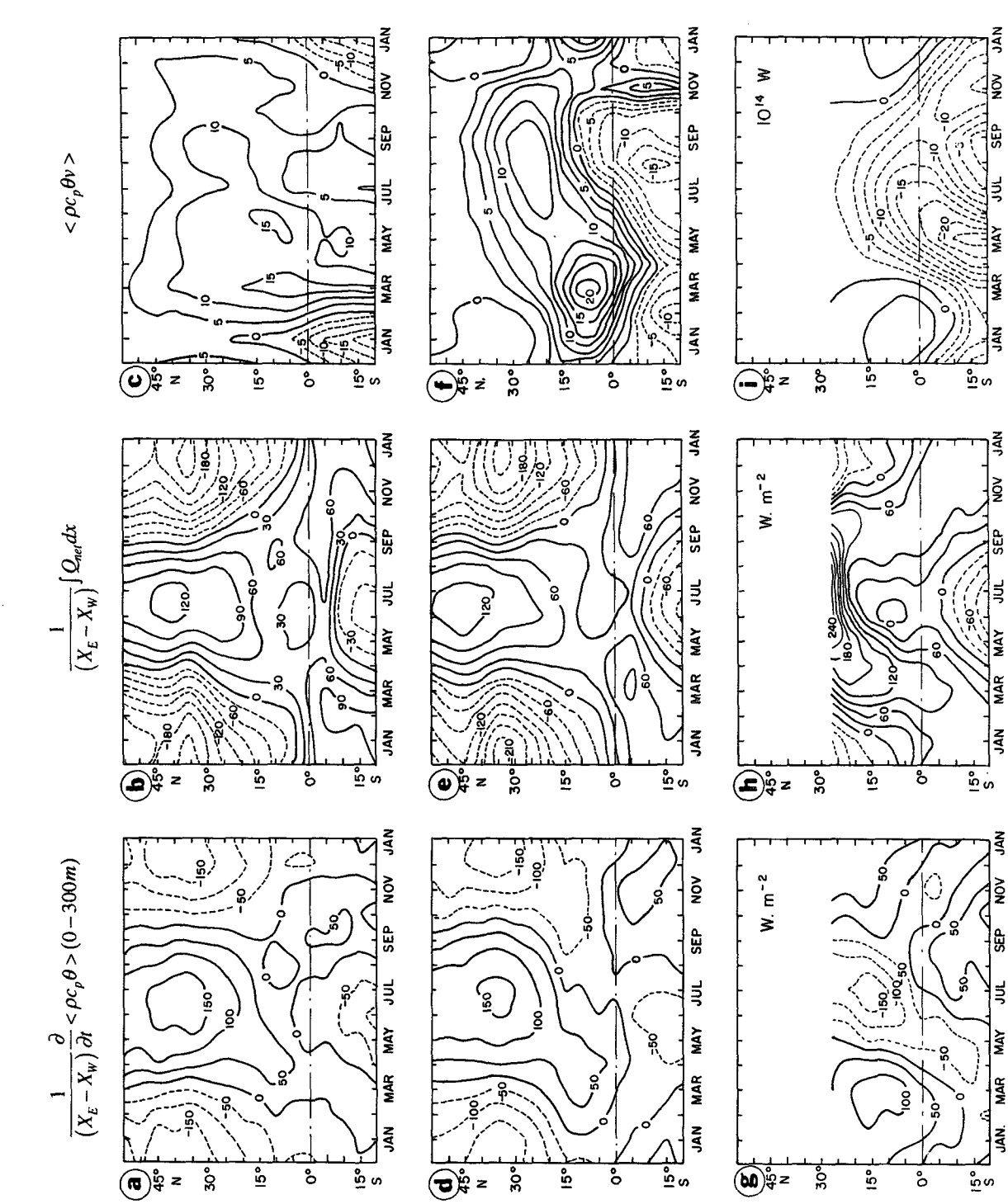

FIG. 17. Terms of the integrated heat budget as a function of time and latitude as redrawn from Hsiung et al. (1989) for the Atlantic (upper panels), the Pacific (middle panels), and the Indian Ocean (lower panels). Note that, north of 5°–10°S, the pattern of rate of change of heat content for the Indian Ocean is out of phase with the patterns for the Atlantic and Pacific Oceans. In the Indian Ocean, therefore, the divergence of heat transport tends to be the sum rather than the difference of two large terms, and the heat transport estimated by integrating this divergence southward should be less in error than in the other oceans.

and Greischar's (1993) recent work, a northward heat transport of order 1 pW should occur at 5°S in December–January (their Fig. 8b). At that time the northward surface flow in the model is only about 5×10^6 m^3 s^{-1} (Fig. 11e), that is, it is weaker than the August surface flow by a factor of 3. That factor of 3 is realistic: it reflects the ratio between the weaker February Ekman flow and its August counterpart (Fig. 7a). It is important to realize how difficult it is to transport 1 pW northward with only 5×10^6 m^3 s^{-1} of surface flow at 27.5°C: if no additional cell is involved, this flow would have to be returned southward at −22.5°C! The model, given its additional 15×10^6 m^3 s^{-1} cell of northward intermediate (12.5°C) and deep (2.5°C) flows, can return the 5×10^6 m^3 s^{-1} of surface flow at the far more acceptable value of 2.5°C.

d. Diabatic processes in the model

One reason for wanting to assess the role of diabatic processes in the model is the suspicion that, as first pointed out by Veronis (1975), these processes are overestimated given the parameterizations of diffusion chosen for the simulation. In the numerical model, diffusion of temperature and salt occurs horizontally and vertically rather than along and across isopycnals. The ratio between horizontal and vertical grid size is reflected in the ratio between the effective turbulent coefficients for horizontal and vertical diffusion, which makes horizontal diffusion much more efficient than vertical diffusion. In regions of mostly flat isotherms, the weak vertical component of diffusion simulates a weak cross-isotherm exchange. In regions of strongly tilted isotherms, the stronger horizontal component necessarily produces a stronger cross-isotherm exchange. Where isothermal and isopycnal surfaces are parallel, entrainment is thus likely to be overestimated. This leads us to suspect that more entrainment than is physically realistic occurs in the model in the regions of upwelling and downwelling described above, an added uncertainty on the strength and depth of penetration of the simulated overturning cells. The problem, however, is likely to affect the annual mean more than the seasonal cells. Let us reconsider Figs. 11e–f. We already emphasized the difference between the streamlines shown and water parcels trajectories: for instance, the spectacular February pattern of continuous downwelling between 25°C and 5°C near 5°N did not imply that individual water parcels sink abruptly 3000 m. Here we wish to point out that it does not imply either that individual water parcels cool from 25°C to 5°C. Figure 11e simply shows that downward motion dominates the zonally integrated velocity in the 25°–20°C, 20°–15°C, 15°–10°C, 10°–5°C temperature ranges, independently of where in the zonal section that downwelling occurs. Conversion of warm to cold water can occur but is not necessary. In fact, it will not occur if isothermal surfaces are displaced vertically at the same rate as water parcels (e.g., by 10 m mo^{-1}, see end of section 3b).

To illustrate this and come back to our distinction between diabatic and adiabatic ways to transport heat, let us consider, rather than the zonally integrated heat equation of section 2b, the model local temperature equation:

$$\frac{\partial \theta}{\partial t} + \mathbf{u}\cdot\nabla\theta = A_H\nabla_H^2\theta + \frac{\partial}{\partial z}\left(\kappa\frac{\partial \theta}{\partial z}\right) = \text{diff},$$

where $\mathbf{u}$ is the 3D model velocity, $\nabla = (\partial/\partial x, \partial/\partial y, \partial/\partial z)$, and $\nabla_H^2 = \partial^2/\partial x^2 + \partial^2/\partial y^2$.

Dividing through by the absolute value of $\nabla\theta$ (at levels where $|\nabla\theta| \neq 0$), we can rewrite this equation in velocity unit as

$$\frac{1}{|\nabla\theta|}\frac{\partial \theta}{\partial t} + \mathbf{u}\cdot\frac{\nabla\theta}{|\nabla\theta|} = \frac{\text{diff}}{|\nabla\theta|},$$

where the term $\mathbf{u}\cdot\nabla\theta/|\nabla\theta| = w_p$ represents by construction the component of velocity perpendicular to the local isothermal surface. Now we can subdivide w_p into "adiabatic" and "diabatic" components ($w_p = w_a + w_d$) by defining w_a and w_d from the following balances[14]:

$$\frac{1}{|\nabla\theta|}\frac{\partial \theta}{\partial t} + w_a = 0$$

$$w_d = \frac{\text{diff}}{|\nabla\theta|}.$$

(One recovers the previous equation by summing the last two.) In the direction perpendicular to a given isothermal surface, w_p represents the volume of water (per unit surface) in motion, w_a the fraction of that volume that "pushes" the isothermal surface ahead, and w_d the fraction that warms or cools during the motion, that is, the fraction that "crosses" the isothermal surface because of diffusion. We can call w_d a "diffusive" or "cross-isotherm" or "entrainment" velocity. As shown schematically in Fig. 18, temperature can change locally through (a) purely adiabatic processes ($\partial\theta/\partial t = -w_p|\nabla\theta|$, when $w_d = 0$, i.e., when $w_p = w_a$), or through (b) purely diffusive processes ($\partial\theta/\partial t = w_d|\nabla\theta|$, when $w_p = 0$, i.e., when $w_a = -w_d$). Typically both processes occur simultaneously and temperature varies according to the dominant one, or temperature remains constant if $w_a = 0$, that is, if $w_p = w_d$. Globally integrated over a basin open only to the south, this last balance corresponds to an equilibrium between

[14] This type of decomposition and the following reasoning will look familiar to those accustomed to working in isopycnal coordinates, and, as pointed out by one of the reviewers, our w_d may be reminiscent of McDougall's dianeutral velocity (McDougall 1987; You et al. 1995). What matters for heat transport, however, are strictly exchanges across isothermal surfaces, which do not a priori coincide with isopycnal or neutral surfaces. Our w_d is therefore not the same quantity as McDougall's dianeutral velocity.

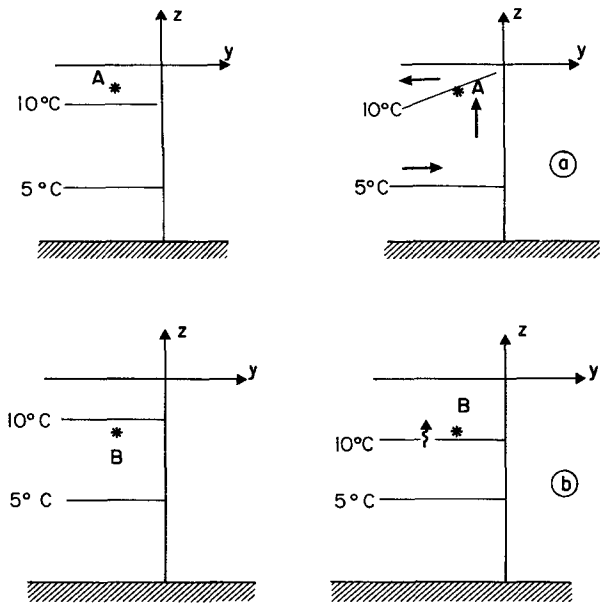

FIG. 18. Schematics of (a) a case of purely advective (adiabatic) cooling and (b) a case of purely diffusive (diabatic) warming. Starting from the initial state pictured in the left panels, point *A* (a) cools as warm surface water leaves the region to be replaced by imported cold water. No diffusive flux is involved. With the notations introduced in the text, the corresponding temperature equation can be written

$$\text{Point } \mathbf{A}: \frac{\partial \theta}{\partial t} = -w_a |\nabla \theta| \quad \text{with} \quad w_a > 0 \quad \text{and} \quad w_d = 0.$$

Point *B* (b) warms as the volume of warm water increases under the action of local diffusive fluxes. No volume transport of either warm or cold water in or out of the region is involved. The corresponding temperature equation can be written

$$\text{Point } \mathbf{B}: \frac{\partial \theta}{\partial t} = w_d |\nabla \theta| \quad \text{with} \quad w_d > 0 \quad \text{and} \quad w_p = 0.$$

heat transport through the southern boundary and net exchange through the surface.

Let us reconsider the annual-mean meridional streamfunction (Fig. 15). Since $\partial\theta/\partial t = 0$ on the annual mean, the situation corresponds to the case $w_d = w_p$, and one can interpret the upwelling in the upper 500 m as (the vertical component of) either the advective or the "diffusive" velocity. This is simply stating that, for a steady state to exist, water locally cooled by advection is being warmed at an equal rate by diffusion. Equivalently one can think of the isotherms as frozen in space, and of the upwelled water as in effect "crossing" them. We insist on this well-known interpretation of the annual mean streamfunction for two reasons. First, it illustrates our concern with the amount of diffusion taking place in the model: the dimensions of the annual meridional cell is conditioned by diffusion. Second, it offers an interesting contrast with the interpretation of the seasonal cells. On a monthly basis, w_p needs not be equal to w_d, it can be mostly balanced by $-(1/|\nabla\theta|)\partial\theta/\partial t$, indicating a global motion of the isotherms themselves. Our purpose is then to quantify the amount of diffusion associated with the vertical motions of Figs. 11e, f. In particular, how much conversion of warm to cold water is concomitant with the spectacular February downwelling? We expect to find horizontal diffusion dominate over vertical diffusion away from the surface [since the Richardson number dependent vertical eddy diffusivity used in the model (appendix A) rapidly drops with depth to its molecular value] and horizontal diffusion to be particularly important close to boundaries where isotherms tilt is increased.

Our once-monthly instantaneous model output does not allow the determination of the instantaneous local rate of change of temperature, but it allows the computation of w, w_p, and w_d (hence w_a by subtraction) using the relevant fields. Because of the instantaneous character of the output, and despite care in adopting the same numerical schemes as those used in the model integration, the obtained fields are quite noisy. We therefore limit the discussion to the most salient results, a more thorough analysis requiring a better suited output. Since our focus is to understand better the February and August streamfunctions of Fig. 11, we limit our attention to processes occurring at the level of the 20°C and 5°C isotherms (which correspond roughly to processes occurring at the 106-m and 979-m model levels), and we define two main latitude ranges of interest: 5°S–5°N and 5°–20°N. This choice allows us to look in more detail at the downwelling occurring in February at the 5°C level in the equatorial region and at the upwelling occurring in August at the 20°C level north of 5°N. The necessary fields (advection of temperature, horizontal and vertical diffusion, and the corresponding advective and diffusive velocities w_p and w_d) were computed at each point, integrated over the above latitudinal ranges to reduce noisiness, and finally accumulated zonally from the western boundary eastward in order to locate where they contribute most to the zonal integral. The results for w_p and w_d will thus be presented in units of volume transport. Note that various choices of finite differencing and smoothing are possible for the computation of $|\nabla\theta|$. This introduces an uncertainty in the estimates of w_p and w_d individually, but not in their ratio, which is the quantity of most interest.

The analysis of the model results confirms that, at the levels considered, vertical diffusion is negligible compared to horizontal diffusion. Therefore, diffusive cooling occurs as easily as diffusive warming: warm bowls are cooled and cool ridges are warmed by horizontal diffusion across the sides of such structures. There are wide regions where w_d is negligible compared to w_p, that is, where temperature changes purely adiabatically, but none where w_d dominates. At the main upwelling and downwelling locations, w_d tends to have the same sign as w_p, implying a tendency for diffusive and advective effects to somewhat compensate each other. In August, w_d can reach $w_p/2$, that is,

have an amplitude similar to that of the adiabatic velocity w_a, while in February w_d remains less than $w_p/4$. The spectacular February downwelling has therefore a mostly adiabatic nature. Our final general remark concerns horizontal diffusion, associated, as we have seen, with topographic features of the isothermal surfaces. Contrary to our original suspicions, it is actually in the middle of the basins and not close to boundaries that isothermal curvature gives rise to maximum horizontal diffusion. These general results are now illustrated in more detail.

1) Processes at the level of the 20°C isotherm between 5°N and 20°N

This is where the model simulates strong upwelling in August (Fig. 11f) and weak downwelling in February (Fig. 11e). Figures 19 and 20, which concern August and February respectively, present the topography of the 20°C isotherm (a), the temperature at the 106-m model level (b), zonally accumulated profiles[15] of horizontal diffusion[16] (c), and zonally accumulated profiles of the velocities perpendicular to and across the 20°C isothermal surface, w_p and w_d (d).

In August, upwelling (solid curve on Fig. 19d) occurs essentially west of 60°E; it continues to the east but with a lesser amplitude. The region is characterized by a bowl of warm water centered near 60°E in the Arabian Sea, and a ridge of colder water centered around India (Figs. 19a,b), a pattern quite reminiscent of that of mixed layer depth, as estimated by Rao et al. (1989). As a consequence, diffusion (dominated by its horizontal component) tends to cool the bowl west of 70°E and warm the ridge between 70° and 90°E; indeed Fig. 19c shows a mostly negative slope west of 70°E, a mostly positive slope east of 70°E. Diffusion close to lateral boundaries does not dominate the integral. The dotted curve on Fig. 19d represents the zonally accumulated profile of the diffusive velocity w_d. Here, w_d has the sign of $A_H\nabla_H^2\theta$ but, because of the modulation by $|\nabla\theta|$, its zonally accumulated profile is dominated by a small-scale diffusive warming between 55° and 60°E. The figure illustrates that the integrated w_d is overall of the same sign as but about a factor 2 smaller than the integrated w_p. The upward motion in the direction perpendicular to the 20°C isothermal surface occurs for about half (12×10^6 m^3 s^{-1}) across the isotherm, half (16×10^6 m^3 s^{-1}) adiabatically, the net result being adiabatic cooling, occurring for the most part near 55°E.

In February downwelling at the 20°C level occurs across the Arabian Sea west of 75°E, tempered by weaker upwelling to the east (Fig. 20d, solid curve). The temperature structure is dominated by a single warm bowl centered around India [Figs. 20a,b, again reminiscent of the mixed layer depth pattern from Rao et al. (1989)], resulting in diffusive cooling between 65°E and 95°E (Fig. 20c). Figure 20d shows that, west of 75°E where the downwelling occurs, no sizeable cross-isotherm flow takes place and temperature therefore changes purely adiabatically. East of 75°E, w_d is small and negative while w_p is small and positive, both slightly increasing near 90°E (slopes of opposite sign but of similar amplitude for the continuous and dotted lines). This indicates weak diffusive and stronger adiabatic cooling. The net result across the basin, therefore, is adiabatic warming occurring mostly west of 70°E, slightly tempered by diffusive cooling occurring mostly near 90°E, as about 5×10^6 m^3 s^{-1} downwell adiabatically, while only about 2×10^6 m^3 s^{-1} cross the 20°C isothermal surface downward.

What is striking when comparing the topography of the 20°C isotherm in August (Fig. 19a) and in February (Fig. 20a) is how much rougher this topography is in August. Stronger curvatures induce stronger horizontal diffusion, hence the more important role played by diabatic transfers in August than in February in the model. In isopycnal rather than in z coordinates, curvatures would be less. Diabatic transfers would therefore most likely play a lesser role in a model with isopycnal rather than horizontal diffusion.

2) Processes at the level of the 5°C isotherm between 5°S and 5°N

In February, as in August, between 15 and 20×10^6 m^3 s^{-1} downwell east of 70°E (Figs. 21a,b, solid curves). The patterns differ west of 70°E where, in February, an additional net 5×10^6 m^3 s^{-1} downwelling occurs, causing the February zonal integral of w_p to be dominated by downwelling. In August, by contrast, 15×10^6 m^3 s^{-1} upwell west of 70°E, cancelling the 15×10^6 m^3 s^{-1} downwelling east of 70°E. The topography of the 5°C isothermal surface (not shown) does not change much from one season to the next, and thus there is no large variation in the diffusive velocities across 5°C: in both cases, between 5 and 7×10^6 m^3 s^{-1} cross 5°C downward,[17] mostly east of 70°E (Figs. 21a,b, dotted curves) because of negative horizontal diffusion (not shown). The variations at the 5°C level between the two seasons are therefore of a purely advective nature. The net result across the basin is, in February, a 15×10^6 m^3 s^{-1} adiabatic increase of the volume of water warmer than 5°C, that is, adiabatic warming, in August, a 6×10^6 m^3 s^{-1} diabatic increase of the volume of water colder than 5°C, that is, diffusive cooling.

[15] Zonal profiles of quantities integrated between 5° and 20°N and accumulated from the western boundary eastward.

[16] Multiplied by ρc_p to obtain units of W m^{-1}.

[17] On the annual mean, this diffusive cooling is balanced by advective warming, while, in reality, one expects deep cold northward boundary currents corresponding to advective cooling to be balanced by diffusive warming (section 4a).

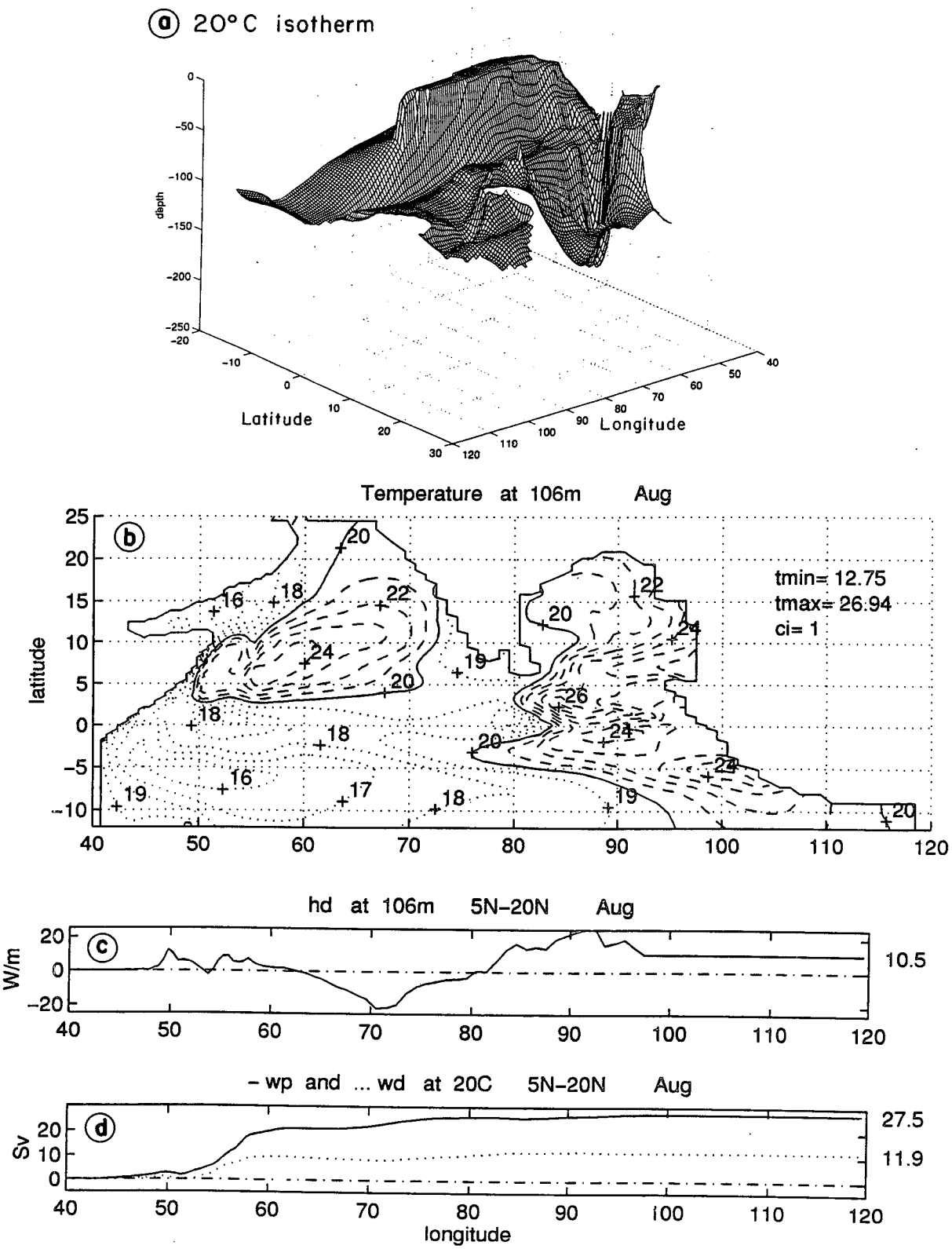

FIG. 19. Localization of diffusive processes between 5° and 20°N in the model in August, near the level of the 20°C isotherm where net upwelling occurs during the southwest monsoon. The upper panel (a) shows the topography of the model 20°C isotherm (a better view was obtained from the northeastern corner of the surface, hence the orientation of the longitude axis from right to left). The middle panel (b) shows a contour plot of temperature at the 106-m model level (contour interval 1°C, temperatures higher than 20°C dashed, temperatures lower than 20°C dotted). The lower panels present zonal profiles of quantities integrated between 5° and 20°N and accumulated from the western boundary eastward, namely (c) $\rho c_p A_H \nabla_H^2 \theta$ at the 106-m level (in W m^{-1}), and (d) w_p, the advective velocity perpendicular to isotherms (solid line), and w_d, the diffusive velocity (dotted line) at the level of the 20°C isotherm (in 10^6 m^3 s^{-1}).

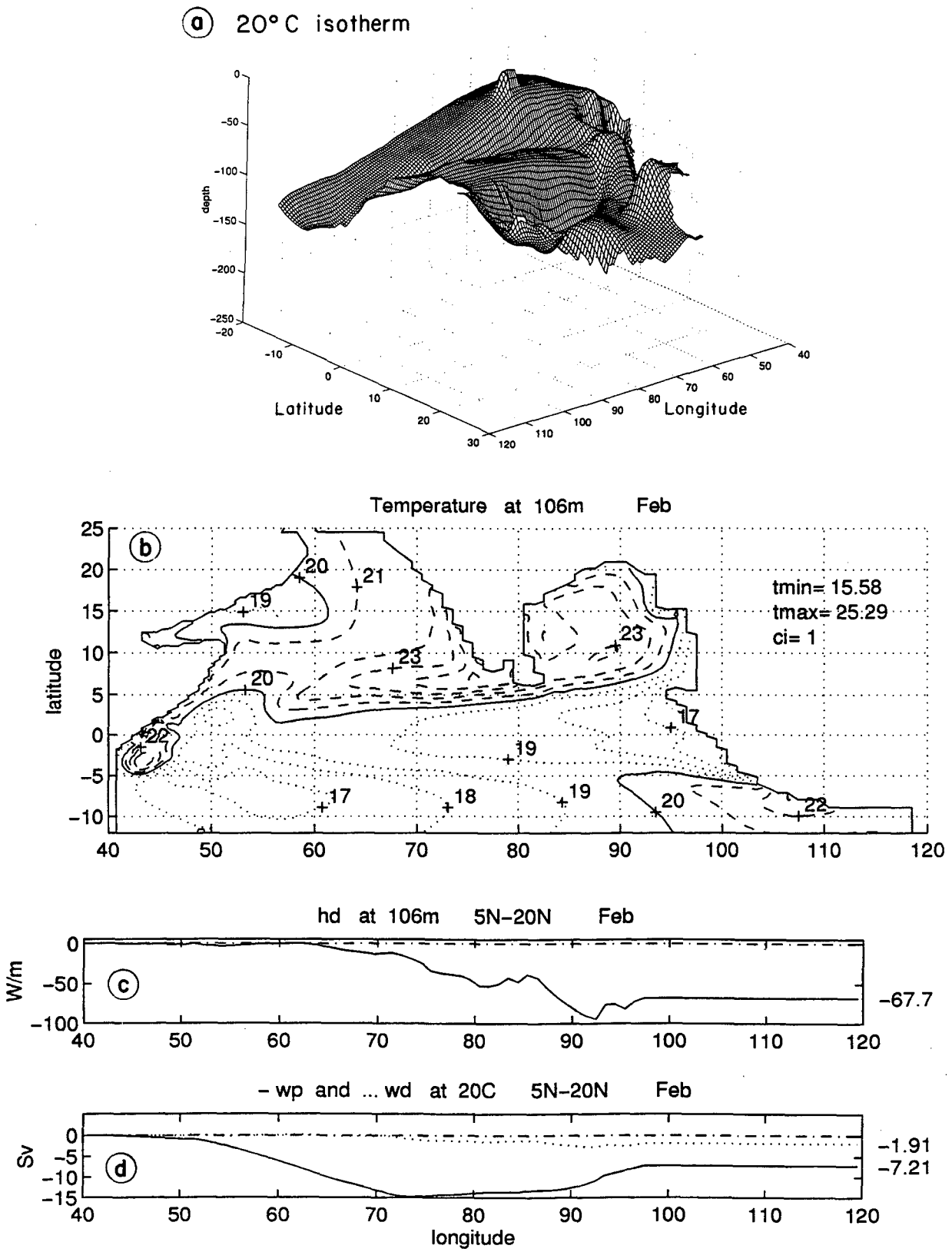

FIG. 20. Localization of diffusive processes between 5° and 20°N in the model in February, near the level of the 20°C isotherm where net downwelling occurs during the northeast monsoon. Same presentation as Fig. 19.

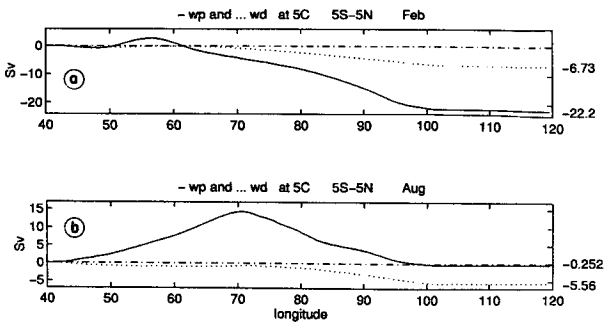

FIG. 21. Localization of diffusive processes between 5°S and 5°N at the level of the 5°C isotherm where there is net downwelling in February (a) and net upwelling in August (b). Same presentation as in Figs. 19d and 20d.

3) SUMMARY IN TERMS OF EQUIVALENT STREAMFUNCTIONS

The above results are summarized in Fig. 22, which represents the quantity

$$-\int_{y}^{Y_N}\int_{X_W}^{X_E}\omega_{\theta=cst}dxdy'$$

ω being equal to (left) w_p, the advective velocity in the direction perpendicular to the isotherms, and (right) w_d, the cross-isotherm velocity, for (upper panels) February and (lower panels) August. In other words, w_p and w_d are locally multiplied by a horizontal surface element centered on $\theta = cst$, and the result is accumulated across the basin and from the north southward. Where the area of isothermal surfaces is close to that of neighboring horizontal surfaces, w_p is close to w and $(-\int_y^{Y_N}\int_{X_W}^{X_E}(w_p)_{\theta=cst}dxdy')$ should be close to the meridional streamfunction $\Psi(y, \theta)$ computed earlier from v binned into temperature classes (section 3a), hence the title "equivalent streamfunction." As long as one restricts the computation to temperatures less than about 22°C, there is indeed a close resemblance between Figs. 22a and 11e, and between Figs. 22c and 11f (giving confidence in choices made for the $|\nabla\theta|$ computation, see above). Near the surface where isothermal surfaces outcrop and where w_p becomes horizontal, the interpretation of the computation in terms of a streamfunction fails. To pursue the analogy, one would need to multiply w_p by a surface element belonging to the local isothermal surface before accumulating. This was not attempted. Figures 22b and 22d allow one to visualize and quantify in a similar fashion the zonally integrated effect of internal diffusion in the y-θ plane. Figure 22 can be thought of as comparing the rate of change of water volumes above given isotherms (a–c) with what could be predicted from diffusive processes (b–d). Subtracting the two would allow one to picture the fraction due to isotherm displacement. Net transport values differ from those of Figs. 20 and 21 because the meridional integration is not done over equivalent latitude bands.

In August (lower panels), the w_d pattern (d) is similar to the w_p pattern (c): weak downwelling cell below 10°C north of 10°S, strong upwelling cell elsewhere, implying the tendency mentioned above for diffusive effects to partly balance the advective effects. The strength of the upwelling "diffusive cell" is, however, about half the strength of the advective cell. In February, there is overall less similarity than in August between the $y-\theta$ patterns of the integrated w_p and w_d. In particular, there is only a weak downwelling "diffusive cell" north of 5°S, limited to temperatures less than 10°C. Above and to the south, the effects of advection and diffusion are additive, diffusive processes being, however, much weaker than advective (and thus than adiabatic) processes. Note that this presentation allows an estimated value of 0.1 pW for the heat transport associated with the downwelling diffusive cell centered at 5°S below 10°C, considering an average 5×10^6 $m^3\ s^{-1}$ cell and a 5°C temperature difference. Pursuing this type of analysis in the future may allow the adiabatic and diabatic heat transports discussed in appendix B to be quantified.

e. Possible impact of the Indonesian Throughflow

The impact on the heat transport of having blocked the Indonesian Throughflow in the model cannot be fully assessed without appropriately designed additional runs (see Godfrey and Weaver 1991). We can, however, make the following remarks. The throughflow [the net amplitude and seasonal variations of which are still under debate (Fieux et al. 1994)] concerns the upper layers near 10°S, where the surface flow is uniformly southward in August, but diverges to the north in February. The throughflow participates in the meridional divergence of heat transport if its transport-averaged temperature changes between its entry point into a given region and its exit point. Concerning our 15°S–20°N model domain then, the throughflow is less likely to have an impact on the meridional heat transport divergence in August than in February. This is because, in August, the injected volume of relatively warm water will probably be swept southward by the wind-driven main circulation of the Indian Ocean, leaving the 10°S–20°N region unaffected, and the 15°S–10°S region affected only to the extent that surface heat fluxes cool the water appreciably between 10°S and 15°S. Thus, taking 10×10^6 $m^3\ s^{-1}$ as an order of magnitude of the throughflow transport, an unlikely 10°C cooling between 10°S and 15°S would be required for the throughflow to cause an appreciable change in our 1.5 pW estimate of the August heat transport convergence. In February by contrast, the injected water is likely to be at least partly swept northward and downward into the 10°S–20°N meridional overturning cell. Given the large temperature difference associated with this overturning, the extra recirculating transport may cause a sizeable increase in the northward heat transport through 10°S. If most of the throughflow adopts

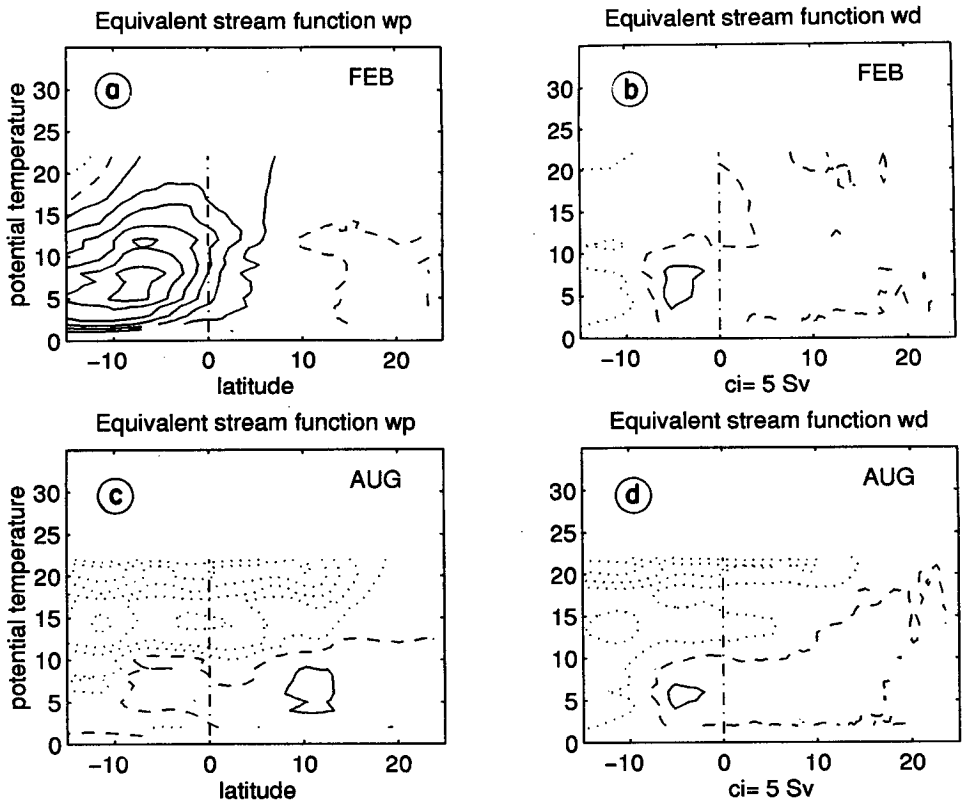

FIG. 22. Equivalent streamfunctions, in $y-\theta$ coordinates, for w_p, the velocity perpendicular to isotherms (a–c) and for w_d, the cross-isotherm velocity (b–d), computed as $-\int_y^{Y_N}\int_{X_W}^{X_E}\omega_{\theta=cst}dxdy'$. The upper panels concern February, the lower panels August. Restricting the figure to temperatures colder than 22°C where the area of isothermal surfaces is close to that of horizontal surfaces illustrates the resemblance between (a–c) and the meridional streamfunctions of Figs. 11e–f.

this path, then the equivalent volume forced southward through 10°S has a much lower transport-averaged temperature than the August volume and is thus even less likely to cool sufficiently between 10°S and 15°S to introduce a heat transport divergence in that region. This reasoning assumes that the existence of the throughflow would not entirely change the circulation patterns that exist when the throughflow is blocked. This seems a reasonable assumption given the wind-driven character of the Indian Ocean seasonal circulation. Note, however, that, according to Hirst and Godfrey (1993), the Indonesian Throughflow does have an effect on the surface heat flux of the northern Indian Ocean (their Fig. 14), which is small (5 W m^{-2}) on the annual mean, but possibly amounting to 20 W m^{-2} or so in summer. A study of the effect of the Indonesian Throughflow on heat content and heat transport separately may thus prove interesting in the future.

5. Conclusions

Despite obvious flaws of the model, the analysis has revealed aspects of the seasonal cycle of heat transport, which seem sufficiently robust to apply to the real tropical Indian Ocean. The success of the study is essentially due to the fact that integrated quantities such as heat content and heat transport, which we chose to examine, are much less sensitive to model parameterizations than local quantities such as SST or mixed layer depth. The analysis has, in particular, confirmed the important part played by Ekman transport in reversing the direction of the net heat transport (notably in the Arabian Sea) because Ekman transport itself reverses sign seasonally on both sides of the equator in response to the monsoon reversals. We were, however, lead to emphasize that, the Ekman transport having a lesser amplitude during the northeast monsoon than during the southwest monsoon, especially south of 10°N, its change of sign is not sufficient to explain why the heat transport south of the Arabian Sea would keep a similar amplitude when reversing from its August to its February value.

Deeper changes in the circulation as predicted by the simulation must thus occur, and we feel confident that seasonal changes in deep layers are to be expected along western boundaries. This encourages us to believe that the 1984–86 observations by Schott et al. (1989, 1990) of deep current reversals along the So-

mali coast are more representative of a climatological state than the 1987 observations by Warren and Johnson (1992) of no reversal. The boreal winter of 1986/87 may thus have been a time of lesser than normal northward heat transport. What we cannot predict from the model analysis, because we cannot trust enough the model deep circulation, is the precise depth at which these changes occur. It is difficult to base predictions on the temperature differences required to ensure heat transport values of magnitude compatible with observations and model, because of the temperature homogeneity of the deep layers. Observations collected during WOCE, especially at deep moorings close to topographic features, should help settle that issue.

The steps we have taken toward assessing the respective parts played by diabatic and adiabatic processes in transporting heat seasonally remain preliminary, essentially because the output we used had not been designed for such a study. The results are nevertheless very promising, and we wish to promote our approach as a useful addition to the more traditional diagnostics used in model assessment, of particular help for future model intercomparisons. Our analysis confirmed that, in the model, diffusion of temperature is dominated by horizontal diffusion below the surface layers and hence by the curvature of the isothermal surfaces. In particular, the curvature of the 5°C isotherm north of 10°S was diagnosed to induce a year-round diffusive cooling, necessarily balanced on the annual mean by advective warming (Figs. 22b–d, Fig. 15c), whereas observations south of 15°S, as summarized by Warren (1994), predict advective cooling. Overestimated internal model diffusion may thus be responsible for some of the discrepancies between model and observations. On a seasonal basis, however, our analysis showed that advective effects dominate, in particular, in February where the spectacular downwelling revealed by the meridional streamfunction was diagnosed to be essentially adiabatic. Simulations with more sophisticated isopycnal diffusion (see, e.g., Gent et al. 1995) may thus very well produce a more satisfying annual mean than ours but a qualitatively similar seasonal cycle of heat transport.

In view of the shortcomings of the one run we analyzed, how should one design a numerical experiment better suited to address the questions posed? Clearly, it would have to be integrable over a longer time in order to check for trends in heat content and to test the degree of adjustment of the deep layers and the degree of repeatability of the seasonal cycle. Outputs would need to be time averaged to ensure stable estimates of the various terms to be computed. Also, it would be of obvious interest to generate a sequence of runs with various surface boundary conditions to test their impact on the model behavior. For instance, making the shortwave radiation term penetrative and seasonally varying, letting longwave radiation follow a σT^4-like law, allowing high frequencies (important for evaporation) in the wind forcing, would influence Q_{net}, SST, and mixed layer depth: would the impact on seasonal heat transport be indeed weak? Reexamining heat transport processes in a coupled model would be a logical next step. Finally, working in the context of a global model would be well worth exploring in order to investigate the effects of closing or not the throughflow region and the southern boundary.

Acknowledgments. S. Wacongne accomplished the first part of the model analysis in 1990–92 in Kiel, while under contract with the Institut für Meereskunde an der Universität Kiel. She was at the time receiving support from DFG Projekt "Indischer Ozean" SCHO 168/20-1, which also funded a presentation of preliminary results at the Vienna IUGG conference. We thank the organizers of the May 1994 International Conference on Monsoon Variability and Prediction, who published a condensed version of this paper in the proceedings of the conference (WCRP-84, WMO/TD-No. 619). Early conversations with M. Visbeck and G. Philander, more recent ones with S. Godfrey, J. McCreary, and J. Wilkin, and comments on the manuscript by J. Toole, K. Speer, S. Griffies, A. Rosati, and two anonymous reviewers are gratefully acknowledged. We thank also P. Richardson and T. McKee, who made their ship-drift dataset available to F. Schott; P. Doaré, who drafted the figures; and H. Leborgne, who helped with the computation of the diffusion terms and with some of the relevant plots.

APPENDIX A

The Simulation and Its Limitations

The numerical finite-differencing code is that of Bryan (1969). Horizontal friction and diffusion are parameterized via Laplacian terms, with coefficients of horizontal eddy viscosity and diffusivity equal to 2×10^3 m^2 s^{-1} where the horizontal resolution is finest, increasing in proportion with grid spacing elsewhere. Vertical friction and diffusion involve Richardson number–dependent vertical mixing coefficients (Pacanowski and Philander 1981). In the upper 10 m of the model, the coefficient of vertical eddy viscosity has a minimum value of 10^{-4} m^2 s^{-1} to compensate for mixing by the high-frequency wind fluctuations, which are absent from the monthly mean forcing winds (see below). In the deep ocean, where vertical mixing is weak, the vertical mixing coefficients drop to their molecular value (1.34×10^{-6} m^2 s^{-1} for the viscosity, 1.34×10^{-7} m^2 s^{-1} for the diffusivity). Unstable temperature gradients are eliminated instantaneously by mixing vertically to a depth that ensures a stable density gradient.

The simulation includes islands and bottom topography (Fig. 2a). It is limited by a realistic coastline in its northern half and by closed walls at 32°S (where the Indian Ocean in reality is open to the Southern Ocean), and at 119°E (where in reality there exist passages connecting the Indian and the Pacific Oceans). As in sim-

ilar simulations, there is a relaxation layer at the southern boundary (here between 18°S and 32°S) within which the model temperature and salinity are forced back toward the Levitus (1982) climatology (steady below 1500 m) throughout the run. Thus, poleward of 18°S, the equation for temperature includes a term $\gamma(\theta - \theta^*)$, where θ^* is the prescribed monthly mean climatological temperature and γ is a Newtonian cooling coefficient equal to 1/(2 days) near the zonal boundary. This is meant to attenuate the effect of the closed wall by maintaining realistic geostrophic heat and mass fluxes through 18°S. One should therefore think of 15°S as the southern limit of the tropical Indian Ocean simulation, and of the band 15°S–32°S as the "rest of the world ocean" where all water mass conversion necessary to close the circulation takes place. Between the two, a "thermohaline circulation" exists that can carry heat southward through 15°S, an important provision since the Indian Ocean is subjected to a net energy influx over the year.

In order to resolve the swift variable currents along the slanted western boundary and along the equator, horizontal resolution is finest between 40°E and 60°E (1/2° long) and between 5°S and 15°N (1/3° lat). Resolution decreases to 1° longitude east of 70°E, to 1° in latitude in the northern Arabian Sea and to 2.5° in latitude at 20°S (Fig. 2b). Vertical resolution is 10 m in the upper 100 m, dropping to 650 m below 2000 m.

The run was started from a state of no motion and an imposed stratification: the Levitus (1982) climatological fields of January temperature and winter salinity. Hellerman and Rosenstein's (1983) climatological monthly wind stresses were used for the dynamical forcing at the surface. Of the four components constituting the net heat flux $Q_{\text{net}} = Q_{\text{SW}} - Q_{\text{LW}} - Q_S - Q_E$ across the ocean surface, the two radiative terms were taken to be constant (in space and time) over the domain of interest: the incoming shortwave $Q_{\text{SW}} = 240$ W m^{-2} and the outgoing longwave $Q_{\text{LW}} = 55$ W m^{-2} (same numerical values as for the tropical Atlantic and Pacific runs). The other two, the sensible and the latent heat fluxes Q_S and Q_E, were computed internally using bulk transfer formulas and Oort's (1983) climatological monthly air temperatures, with specific humidity held constant.[18] Because the dominant terms are the shortwave radiation, which is constant, and the latent heat flux, which varies, variations in Q_{net} in the model essentially reflect variations in the latent heat flux. Despite the choice of a constant value for shortwave radiation, distinction between a winter and a summer hemisphere at any time does arise from the meridional asymmetries in the imposed air temperature. As pointed out by one of the reviewers, taking Q_{SW} as a constant is not a satisfying simplification since, in reality, Q_{SW} and Q_E vary seasonally with similar amplitudes. As a consequence, the pattern of seasonal variations of the model's Q_{net} will be seen to exhibit flaws when compared to estimates from observations (section 2b, Figs. 5a–c). The only rationale for choosing constant radiative terms was simplicity. More elaborate parameterizations involving cloud physics have since been developed. Their impact on Q_{net} and heat transport will be worth exploring in the future but are likely to be of secondary importance compared to adiabatic effects. No attempt was made to impose (or simulate the effects of) freshwater fluxes.[19]

Simulating a realistic deep circulation may be important for the meridional heat transport since, according to estimates at 32°S (Toole and Warren 1993), it involves cold northward deep western boundary currents and warmer southward return flow. In the model, the deep circulation arises through geostrophic adjustment to the initial stratification (timescale one inertial period) and through continuous temperature and salinity forcing at the southern boundary. Longer planetary wave adjustment can also take place in case of discrepancies between the topography implicit in Levitus climatology and that in the model. The deep circulation may subsequently change through barotropic adjustment to the monthly varying surface wind forcing (instantaneously under the rigid lid assumption) or because of seasonal net convergences and divergences within the layers above. How realistic a deep circulation can one expect? Vertical resolution is limiting: there are only two model levels below 3000 m, with the bottom no deeper than 4149 m, so that some of the bottom circulation is necessarily missing (the coldest temperatures of the model basin are around 0.95°C). The quality of the initial stratification and that of the temperature and salinity fields used subsequently for the restoring condition at the southern boundary is also limiting: observations are particularly sparse in the 15°–32°S region [Figs. 6–10 in Levitus (1982)]. Even though the interior stratification is free to adjust to the circulation past the initial instant, which typically leads

[18] Here, $Q_S = \rho C_D C_p V(T_0 - T_A)$, with $\rho = 1200$ kg m^{-3}, $C_D = 1.4 \times 10^{-3}$, $C_p = 10^3$ J kg^{-1} °C^{-1}; $Q_E = \rho C_D L V[e_S(T_0) - \gamma e_S(T_A)](0.622/p_A)$, with $L = 2.49 \times 10^6$ J kg^{-1}, $p_A = 1013$ hPa. V is the surface wind speed, T_0 the sea surface temperature, T_A the atmospheric temperature at the sea surface, $e_S(T)$ is the saturation vapor pressure $e_S(T) = 10^{[9.4-(2353/T)]}$, and γ the relative humidity, assigned the constant value 0.8. To parameterize evaporation caused by high-frequency wind fluctuations that are absent from the mean monthly winds, wind speeds lower than 4.8 m s^{-1} are replaced by the value 4.8 m s^{-1} in the formula for Q_E. This avoids excessively high temperatures in regions of weak winds.

[19] The initially imposed salinity field changes only through diffusion and advection by the seasonal currents. Gradients within the uppermost layers where diffusion is most important tend to erode, and the surface salinity becomes unrealistic during the model run. Changes below occur mostly through advection and the subsurface salinity field remains meaningful (e.g., horizontal maps of the model salinity at 75 m do show low salinity waters invading the western coast of the Arabian Sea during the southwest monsoon). The assumption made here is that, although salinity does enter the dynamics through density, its exact value close to the surface is not crucial.

to horizontal gradients sharper than those in the climatology (see Semtner and Chervin 1992; Matano and Philander 1993), the strength of the deep currents is likely to be underestimated. This is of negligible consequence if one focuses on the seasonal cycle of the circulation in the upper layers but of potential importance for the analysis of the meridional heat transport: underestimating the strength of the deep currents may imply underestimating the strength of the warmer return flow and thus underestimating the model annual mean meridional heat transport. The seasonal cycle of that transport may, however, be realistic. One expects seasonal variations to affect mostly the upper layers and, even in the case of large variations of mass transport in the deep layers, details may not matter because of the overall small transport-averaged temperature involved. The seasonal cycle of heat transport is therefore more likely to be influenced by weaknesses in the parameterization of the surface heat fluxes than by weaknesses in the resolution of the deep circulation.

A final remark on the way the model (written on a B-grid) treats vertical advection needs to be made. In the version we used, as in most versions until recently, there are two distinct fields of vertical velocity w carrying the momentum and the tracers. It has been remarked that these fields differ from each other, that they are quite noisy and that spurious vertical advection of momentum can occur (Tréguier 1992, personal communication). Clearly, when dealing with temperature advection, care must be taken to define the proper vertical velocity. The problem is that the noisiness in w might affect the way the model transports heat, through correlations with a similarly noisy temperature field. Because, however, the temperature field is not noisy (even instantaneously), this point should be of no concern.

APPENDIX B

Adiabatic and Diabatic Components of the Heat Transport

Let us rewrite the instantaneous heat budget integrated from the northern boundary to the latitude y schematically as

$$\frac{\partial}{\partial t}\mathrm{HC}(y,t) - \mathrm{HT}(y,t) = \mathrm{HF}(y,t),$$

where HC represents the heat content and HF the net surface heat flux into the ocean north of y, HT represents the heat transport (positive to the north) through y, and diffusive fluxes through y have been neglected. Averaged in time over a year, this equation reduces to $-[\mathrm{HT}]_{av} = [\mathrm{HF}]_{av}$, a purely diabatic balance expressing that, in the presence of a nonzero net heat flux through the ocean surface north of y, temperature conversion must occur somewhere in the domain, and thus an advective heat transport must exist through y to maintain the temperature structure in steady state. By estimating the annual-mean model heat transport, we have thus estimated the annual-mean component of our diabatic heat transport. For instance, at 5°N, we have estimated an annual-mean transport of -1.5×10^{14} W (Fig. 6), a small value compared to the instantaneous values of 10×10^{14} W in February and -10×10^{14} W in August (Fig. 5g). Let us reconsider the total instantaneous heat transport; it can have a diabatic component different from $[\mathrm{HT}]_{av}$. In other words, there is no reason to expect all the time-varying part of the heat transport to be adiabatic. The real issue, then, is to assess the respective importance of diabatic and adiabatic processes in the time-varying part of the net heat transport. One would thus like to split the fields into annual means and fluctuations with respect to that mean (and, ideally, to split even further into monthly means and fluctuations at a shorter period, in order to distinguish purely seasonal from eddy effects). As already mentioned, our once-a-month output does not permit this decomposition, and we therefore continue the discussion using instantaneous fields.

Let us now formally split each term of the instantaneous heat budget into two seasonally varying parts and rewrite the budget as

$$\overbrace{\frac{\partial}{\partial t}(\mathrm{HC}^{(1)} + \mathrm{HC}^{(2)})}^{\mathrm{HC}(y,t)} - \overbrace{(\mathrm{HT}^{(1)} + \mathrm{HT}^{(2)})}^{\mathrm{HT}(y,t)} = \overbrace{(\mathrm{HF}^{(1)} + \mathrm{HF}^{(2)})}^{\mathrm{HF}(y,t)}.$$

We define the two components $\mathrm{HF}^{(1)}(y, t)$ and $\mathrm{HF}^{(2)}(y, t)$ of the net surface heat flux so that they are of the same sign and they satisfy the balances

$$\mathrm{HF}^{(1)} = -\mathrm{HT}^{(1)} \tag{B1}$$

$$\mathrm{HF}^{(2)} = \frac{\partial}{\partial t}\mathrm{HC}^{(1)}. \tag{B2}$$

Necessarily then, the remaining components of the heat transport and of the rate of change of heat content satisfy

$$\frac{\partial}{\partial t}\mathrm{HC}^{(2)} = \mathrm{HT}^{(2)}. \tag{B3}$$

This decomposition allows us to identify our diabatic heat transport with $\mathrm{HT}^{(B1)}$ [balance (B1) is of the same nature as the annual-mean heat balance], and our adiabatic heat transport with $\mathrm{HT}^{(2)}$ [balance (B3) quantifies the role of the circulation in changing the heat content adiabatically]. The remaining nonadvective balance (B2) quantifies the rate of change of heat content caused by surface heating. By time-averaging these balances, we check that

$$-[\mathrm{HT}^{(1)}]_{av} = [\mathrm{HF}^{(1)}]_{av}$$

$$\text{and} \quad [\mathrm{HT}^{(2)}]_{av} = [\mathrm{HF}^{(2)}]_{av} = 0,$$

and, therefore, that

$$[\mathrm{HT}^{(1)}]_{av} = [\mathrm{HT}]_{av} \quad \text{and} \quad [\mathrm{HF}^{(1)}]_{av} = [\mathrm{HF}]_{av}.$$

We can use the above formalism to summarize certain necessary relationships among the various terms of the split heat budget. First, we remark that, given our definitions, $\mathrm{HF}^{(1)}$, $\mathrm{HF}^{(2)}$, and thus $(\partial/\partial t)\mathrm{HC}^{(1)}$ have the same sign as HF, while $\mathrm{HT}^{(1)}$ has the opposite sign. One straightforward consequence is that, in absolute value, the diabatic heat transport ($|\mathrm{HT}^{(1)}| = |\mathrm{HF}^{(1)}|$) must always be less than the net surface flux $|\mathrm{HF}|$, because $|\mathrm{HF}^{(1)}|$ is less than $|\mathrm{HF}|$ (provided $\mathrm{HF}^{(2)} \neq 0$). By contrast, the sign of $(\partial/\partial t)\mathrm{HC}^{(2)}$, equal by construction to the sign of $\mathrm{HT}^{(2)}$, is a priori unrelated to that of HF. Formally, the case $\mathrm{HF}^{(2)} = 0$ is possible. Since $[\mathrm{HF}^{(2)}]_{av} = 0$, $\mathrm{HF}^{(2)}$ must change sign throughout the year. If, therefore, the sign of HF does not change, $\mathrm{HF}^{(2)}$, and thus $(\partial/\partial t)\mathrm{HC}^{(1)}$, have to be zero. In such a case, $\mathrm{HF} = \mathrm{HF}^{(1)}$, and the diabatic heat transport $\mathrm{HT}^{(1)}(y, t)$ is directly measured by the net surface heat flux $-\mathrm{HF}(y, t)$ (as if the annual mean balance held instantaneously). Still in that case, $(\partial/\partial t)\mathrm{HC}^{(2)} = (\partial/\partial t)\mathrm{HC}$, and the adiabatic heat transport $\mathrm{HT}^{(2)}(y, t)$ is directly measured by the total rate of change of heat content $(\partial/\partial t)\mathrm{HC}(y, t)$. The original thing about the northern Indian Ocean, however, as mentioned in the introduction, is that, at the peak of the southwest and northeast monsoons, the total rate of change of heat content $(\partial/\partial t)\mathrm{HC}$ and the net surface heat flux HF have opposite signs. At these times then, $(\partial/\partial t)\mathrm{HC}^{(2)}$ and thus $\mathrm{HT}^{(2)}$ on the one hand, and HF and thus $(\partial/\partial t)\mathrm{HC}^{(1)}$ on the other, necessarily have opposite signs. As a consequence, in absolute value, the adiabatic heat transport ($|\mathrm{HT}^{(2)}| = |(\partial/\partial t)\mathrm{HC}^{(2)}|$) is necessarily greater than the total rate of change of heat content $|(\partial/\partial t)\mathrm{HC}|$, because $|(\partial/\partial t)\mathrm{HC}|$ is less than $|(\partial/\partial t)\mathrm{HC}^{(2)}|$. This is saying that, in August, for instance, when the net surface heat flux is into the northern Indian Ocean—that is, is positive—the fraction $\mathrm{HF}^{(1)}$ induces a southward diabatic heat transport $\mathrm{HT}^{(1)}$, whereas the fraction $\mathrm{HF}^{(2)}$ induces an increase in heat content $(\partial/\partial t)\mathrm{HC}^{(1)}$. The total heat content, however, decreases because the circulation induces a negative $(\partial/\partial t)\mathrm{HC}^{(2)}$, which overwhelms $(\partial/\partial t)\mathrm{HC}^{(1)}$. At such a time therefore, diabatic and adiabatic heat transports are both southward. The reverse is true in January, as summarized by the following inequalities:

- in June–August

$$0 < -\mathrm{HT}^{(1)} = \mathrm{HF}^{(1)} < \mathrm{HF}$$

$$-\mathrm{HF}^{(2)} = -\frac{\partial}{\partial t}\mathrm{HC}^{(1)} < 0 < -\frac{\partial}{\partial t}\mathrm{HC} < -\frac{\partial}{\partial t}\mathrm{HC}^{(2)} = -\mathrm{HT}^{(2)}$$

- in December–February

$$0 < \mathrm{HT}^{(1)} = -\mathrm{HF}^{(1)} < -\mathrm{HF}$$

$$\mathrm{HF}^{(2)} = \frac{\partial}{\partial t}\mathrm{HC}^{(1)} < 0 < \frac{\partial}{\partial t}\mathrm{HC} < \frac{\partial}{\partial t}\mathrm{HC}^{(2)} = \mathrm{HT}^{(2)}.$$

According to Figs. 5a–f, HF and $(\partial/\partial t)\mathrm{HC}$ have the same order of magnitude. It is clear, then, that the adiabatic heat transport $\mathrm{HT}^{(2)}$, which is (in absolute value) at least as large as $(\partial/\partial t)\mathrm{HC}$, represents a sizeable fraction of the total transport (as a consequence, reduced-gravity models devoid of diabatic processes should capture a non-negligible fraction of the seasonal heat transport). Since, however, we do not know at this stage how HF is split into $\mathrm{HF}^{(1)}$ and $\mathrm{HF}^{(2)}$, the relative importance of $\mathrm{HT}^{(1)}$ is not known. This issue is reconsidered in section 4d.

REFERENCES

Böning, C. W., and P. Herrmann, 1994: Annual cycle of poleward heat transport in the ocean: Results from high-resolution modeling of the North and Equatorial Atlantic. *J. Phys. Oceanogr.*, **24,** 91–107.

Bryan, K., 1962: Measurements of meridional heat transport by ocean currents. *J. Geophys. Res.*, **67,** 3403–3414.

——, 1969: A numerical method for the study of the World Ocean. *J. Comput. Phys.*, **4,** 347–376.

Bryden, H. L., D. H. Roemmich, and J. A. Church, 1991: Ocean heat transport across 24°N in the Pacific. *Deep-Sea Res.*, **38,** 297–324.

Cane, M., 1979: The response of an equatorial ocean to simple wind stress patterns. Part II: Numerical results. *J. Mar. Res.*, **37,** 253–299.

Düing, W., and A. Leetmaa, 1980: Arabian Sea cooling: A preliminary heat budget. *J. Phys. Oceanogr.*, **10,** 307–312.

Fieux, M., C. Andrié, P. Delecluse, A. G. Ilahude, A. Kartavtseff, F. Mantisi, R. Molcard, and J. C. Swallow, 1994: Measurements within the Pacific–Indian Oceans throughflow region. *Deep-Sea Res.*, **41,** 1091–1130.

Fu, L. L., 1986: Mass, heat and freshwater fluxes in the south Indian Ocean. *J. Phys. Oceanogr.*, **16,** 1683–1693.

Gent, P. R., J. Willebrand, T. J. McDougall, and J. C. McWilliams, 1995: Parameterizing eddy-induced tracer transports in ocean circulation models. *J. Phys. Oceanogr.*, **25,** 463–474.

Godfrey, J. S., and A. J. Weaver, 1991: Is the Leeuwin Current driven by Pacific heating and winds. *Progress in Oceanography,* Vol. 27, Pergamon, 225–272.

——, A. Alexiou, A. G. Ilahude, D. M. Legler, M. E. Luther, J. P. McCreary Jr., G. A. Meyers, K. Mizuno, R. R. Rao, S. R. Shetye, J. H. Toole, and S. Wacongne, 1995: The role of the Indian Ocean in the global climate system: Recommendations regarding the global ocean observing system. Ocean Observing System Development Panel Rep., Texas A&M University, College Station, TX, 89 pp.

Hastenrath, S., and P. J. Lamb, 1979: *Climatic Atlas of the Indian Ocean. Part I: Surface Climate and Atmospheric Circulation.* The University of Wisconsin Press.

——, and ——, 1980: On the heat budget of hydrosphere and atmosphere in the Indian Ocean. *J. Phys. Oceanogr.*, **10,** 694–708.

——, and L. Greischar, 1993: The monsoonal heat budget of the hydrosphere–atmosphere system in the Indian Ocean sector. *J. Geophys. Res.*, **98,** 6869–6881.

Hellerman, S., and M. Rosenstein, 1983: Normal monthly wind stress over the world ocean with error estimates. *J. Phys. Oceanogr.*, **13,** 1093–1104.

Hirst, C., and J. S. Godfrey, 1993: The role of Indonesian Throughflow in a global ocean GCM. *J. Phys. Oceanogr.*, **23,** 1057–1086.

Hsiung, J., 1985: Estimates of global oceanic meridional heat transport. *J. Phys. Oceanogr.*, **15,** 1405–1413.

——, R. E. Newell, and T. Houghtby, 1989: The annual cycle of oceanic heat storage and oceanic meridional heat transport. *Quart. J. Roy. Meteor. Soc.*, **115,** 1–28.

Leetmaa, A., and H. Stommel, 1980: Equatorial current observations in the western Indian Ocean in 1975 and 1976. *J. Phys. Oceanogr.*, **10,** 258–269.

Levitus, S., 1982: *Climatological Atlas of the World Ocean.* NOAA Prof. Paper No. 13, U.S. Gov. Printing Office, 173 pp.

——, 1984: Annual cycle of temperature and heat storage in the world ocean. *J. Phys. Oceanogr.*, **14,** 727–746.

——, 1987: Meridional Ekman heat fluxes for the world ocean and individual ocean basins. *J. Phys. Oceanogr.*, **17,** 1484–1492.

Luyten, J. R., and J. C. Swallow, 1976: Equatorial undercurrents. *Deep-Sea Res.*, **23,** 999–1001.

Matano, R., and G. Philander, 1993: Heat and mass balances of the South Atlantic Ocean calculated from a numerical model. *J. Geophys. Res.*, **98,** 977–984.

McCreary, J. P., P. K. Kundu, and R. L. Molinari, 1993: A numerical investigation of dynamics, thermodynamics and mixed-layer processes in the Indian Ocean. *Progress in Oceanography,* Vol. 31, Pergamon, 181–244.

McDougall, T. J., 1987: Neutral surfaces. *J. Phys. Oceanogr.*, **17,** 1950–1964.

Mechoso, C. R., A. W. Robertson, N. Barth, M. K. Davey, P. Delecluse, P. R. Gent, S. Ineson, B. Kirtman, M. Latif, H. Le Treut, T. Nagai, J. D. Neelin, S. G. H. Philander, J. Polcher, P. S. Schopf, T. Stockdale, M. J. Suarez, L. Terray, O. Thual, J. J. Tribbia, 1995: The seasonal cycle over the tropical Pacific in general circulation models. *Mon. Wea. Rev.*, **123,** 2825–2838.

Meehl, G. A., W. M. Washington, and A. J. Semtner, 1982: Experiments with a global ocean model driven by observed atmospheric forcing. *J. Phys. Oceanogr.*, **12,** 301–312.

Oort, A. H., 1983: Global atmosphere circulation statistics, 1958–1973. NOAA Prof. Paper No. 14, U.S. Govt. Printing Office, 180 pp.

Pacanowski, R., and S. G. H. Philander, 1981: Parameterization of vertical mixing in numerical models of tropical oceans. *J. Phys. Oceanogr.*, **11,** 1443–1451.

Philander, S. G. H., and R. Pacanowski, 1980: The oceanic response to cross-equatorial winds (with application to coastal upwelling in low latitudes). *Tellus,* **33,** 201–210.

——, and ——, 1986a: A model of the seasonal cycle in the tropical Atlantic Ocean. *J. Geophys. Res.*, **91,** 14 192–14 206.

——, and ——, 1986b: The mass and heat budget in a model of the tropical Atlantic Ocean. *J. Geophys. Res.*, **91,** 14 212–14 220.

——, W. J. Hurlin, and A. D. Seigel, 1987: Simulation of the seasonal cycle of the tropical Pacific Ocean. *J. Phys. Oceanogr.*, **17,** 1986–2002.

Rao, R. R., R. L. Molinari, and J. F. Festa, 1989: Evolution of the climatological near-surface thermal structure of the tropical Indian Ocean. Part 1: Description of mean monthly mixed layer depth, and sea surface temperature, surface current, and surface meteorological fields. *J. Geophys. Res.*, **94,** 10 801–10 815.

Richardson, P. L., and T. K. McKee, 1989: Surface velocity in the equatorial oceans (20°N–20°S) calculated from historical ship drifts. Woods Hole Oceanographic Institution Tech. Rep. WHOI-89-9, 50 pp.

Roemmich, D., 1983: The balance of geostrophic and Ekman transports in the tropical Atlantic Ocean. *J. Phys. Oceanogr.*, **13,** 1534–1539.

Rosati, A., and K. Miyakoda, 1988: A general circulation model for upper ocean simulation. *J. Phys. Oceanogr.*, **18,** 1601–1626.

Schott, F., 1986: Seasonal variation of cross-equatorial flow in the Somali Current. *J. Geophys. Res.*, **91,** 10 581–10 584.

——, M. Fieux, J. Kindle, J. C. Swallow, and R. Zantopp, 1988: The boundary currents east and north of Madagascar. Part II: Direct measurements and model comparisons. *J. Geophys. Res.*, **93,** 4963–4974.

——, J. C. Swallow, and M. Fieux, 1989: Deep currents underneath the equatorial Somali Current. *Deep-Sea Res.*, **36,** 1191–1199.

——, ——, and ——, 1990: The Somali Current at the equator: Annual cycle of currents and transports in the upper 1000 m and connection to neighboring latitudes. *Deep-Sea Res.*, **37,** 1825–1848.

Semtner, A. J., and R. M. Chervin, 1992: Ocean general circulation from a global eddy-resolving model. *J. Geophys. Res.*, **97,** 5493–5550.

Slutz, R. J., S. L. Lubker, J. D. Hiscox, S. D. Woodruff, R. L. Jenne, D. H. Joseph, P. M. Steurer, and J. D. Elms, 1985: Comprehensive Ocean–Atmosphere Data Set. Release 1, 268 pp. [Available from NOAA Environmental Research Laboratory, Climate Research Program, Boulder, CO, 30303.]

Swallow, J. C., F. Schott, and M. Fieux, 1991: Structure and transport of the East African Coastal Current. *J. Geophys. Res.*, **96,** 22 245–22 257.

Toole, J. M., and M. E. Raymer, 1985: Heat and fresh water budgets of the Indian Ocean—Revisited. *Deep-Sea Res.*, **32,** 917–928.

——, and B. A. Warren, 1993: A hydrographic section across the subtropical South Indian Ocean. *Deep-Sea Res.*, **40,** 1973–2019.

Veronis, G., 1975: The role of models in tracer studies. *Numerical Models of the Ocean Circulation,* National Academy of Sciences, 133–146.

Visbeck, M., 1989: Saisonale Analyse des dreidimensionalen GFDL-Zirkulationsmodells im Äquatorialen Indischen Ozean. M.S. thesis, University of Kiel, 73 pp. [Available from Institut für Meereskunde an der Universität Kiel, Düsternbrooker Weg 20, 2300 Kiel 1, Germany.]

——, and F. Schott, 1992: Analysis of seasonal current variations in the western equatorial Indian Ocean: Direct measurements and GFDL model comparison. *J. Phys. Oceanogr.*, **22,** 1112–1128.

Warren, B. A., 1994: Driving the meridional overturning in the Indian Ocean. *Deep-Sea Res.*, **41,** 1349–1360.

——, and G. C. Johnson, 1992: Deep currents in the Arabian Sea in 1987. *Mar. Geol.*, **104,** 279–288.

Wilkin, J. L., J. V. Mansbridge, and J. S. Godfrey, 1995: Pacific Ocean heat transport at 24°N in a high-resolution global model. *J. Phys. Oceanogr.*, **25,** 2204–2214.

Woodberry, K. E., M. E. Luther, and J. J. O'Brien, 1989: The wind-driven seasonal circulation in the southern tropical Indian Ocean. *J. Geophys. Res.*, **94,** 17 985–18 002.

You, Y., T. J. McDougall, and R. W. Schmitt, 1995: Dianeutral motion, water mass conversion, and nonlinear effects on the density ratio in the Pacific thermocline. *J. Phys. Oceanogr.*, **25,** 1891–1904.